

Period spacings of γ Doradus pulsators in the *Kepler* field: Rossby and gravity modes in 82 stars

Gang Li^{1,2*}, Timothy Van Reeth^{1,2}, Timothy R. Bedding^{1,2†}, Simon J. Murphy^{1,2},
Victoria Antoci²

¹*Sydney Institute for Astronomy (SfA), School of Physics, University of Sydney 2006, Australia*

²*Stellar Astrophysics Centre, Department of Physics and Astronomy, Aarhus University, Ny Munkegade 120, DK-8000 Aarhus C, Denmark*

Accepted XXX. Received YYY; in original form ZZZ

ABSTRACT

Rossby modes are the oscillations in a rotating fluid, whose restoring force is the Coriolis force. They provide an additional diagnostic to understand the rotation of stars, which complicates asteroseismic modelling. We report 82 γ Doradus stars for which clear period spacing patterns of both gravity and Rossby modes have been detected. The period spacings of both show a quasi-linear relation with the pulsation period but the slope is negative for the gravity modes and positive for the Rossby modes. Most Rossby modes have $k = -2, m = -1$. For only one star a series of $k = -1, m = -1$ modes is seen. For each pattern, the mean pulsation period, the mean period spacing, and the slope are measured. We find that the slope correlates with the mean period for Rossby mode patterns. The traditional approximation of rotation is used to measure the near-core rotation rate, assuming the star rotates rigidly. We report the near-core rotation rates, the asymptotic period spacings, and the radial orders of excited modes of these 82 main-sequence stars. The near-core rotation rates lie between 0.6 d^{-1} and 2.3 d^{-1} . Six stars show surface rotation modulations, among which only KIC 3341457 shows differential rotation while the other five stars have uniform rotations. The radial orders of excited modes show different distributions for the dipole and quadrupole gravity modes versus the Rossby modes.

Key words: stars: oscillations – stars: rotation – stars: variables

1 INTRODUCTION

Rotation is one of the key parameters that decides how stars evolve, since it affects many physical processes of the stellar interior (e.g. Maeder 2009; Mathis et al. 2013). For example, differential rotation induces an extra shear mixing and changes the local abundances of chemical elements. It can transport fuel into the nuclear burning regions and extend the lifetime of the star (e.g. Van Reeth et al. 2018; Prat et al. 2018). Differential rotation, both in radial and latitudinal directions, has been seen in the Sun and some sun-like stars (e.g. Thompson et al. 1996; Couvidat et al. 2003; Benomar et al. 2018), and A-type main sequence stars (e.g. Hattai et al. 2019). However, our understanding of rotation is still incomplete (e.g. Aerts et al. 2014; Cazorla et al. 2017).

In the rotating frame, the Coriolis force is defined to maintain Newton’s laws of motion. This kind of inertial force acts as the restoring force for Rossby modes (r-modes, Pa-

paloizou & Pringle 1978). Rossby modes are inertial modes, unlike the well-known gravity modes and pressure modes from asteroseismology, whose restoring forces are buoyancy and the pressure gradient, respectively. Rossby modes involve global toroidal motions coupling with the spheroidal motion by the Coriolis force, whose compression and expansion lead to the temperature perturbations and hence make the Rossby modes visible (Pedlosky 1982; Saio et al. 2018a). This wave propagates in the direction retrograde to the rotation and is confined to the mid-latitudes (Saio 1982; Lee & Saio 1997), introducing the possibility of measuring the stellar inclination in future (Saio et al. 2018a). Rossby waves also have discrete frequencies that are smaller than the rotation frequency in the inertial frame (Provost et al. 1981). We refer the interested reader to Saio et al. (2018a), and the references therein, for a more extensive theoretical discussion about r-modes.

Rossby waves are seen or predicted in many types of rotating systems. They appear in planetary atmospheres (Rossby 1939) and play a key role in accurate weather forecasting (e.g. Screen & Simmonds 2014). The Sun rotates

* E-mail: gali8292@uni.sydney.edu.au

† E-mail: tim.bedding@sydney.edu.au

slowly but the Rossby waves still can be observed by tracking the coronal brightpoints and the south-north helioseismic travel times (McIntosh et al. 2017; Löptien et al. 2018; Liang et al. 2018). They have the potential to improve our understanding of energy transfer, solar activity, and space weather (Zaqarashvili et al. 2015). Many questions remain. For example, how do the Rossby waves affect the protoplanetary disc (Lovelace & Romanova 2014) and how do they affect the evolution of DA white dwarfs and neutron stars (Saio 1982; Berthomieu & Provost 1983; Andersson 1998; Brown & Ushomirsky 2000)?

In this paper, we conduct an observational study of γ Doradus stars with resolved gravity and Rossby modes. The brightness variations of γ Dor stars have been observed for several decades (e.g. Cousins & Warren 1963; Balona et al. 1994). They are F to A-type main sequence stars with typical masses between $1.4M_{\odot}$ and $2.0M_{\odot}$, burning hydrogen in their convective cores (Van Reeth et al. 2015b). The pulsations in γ Dor stars are mainly high radial order ($20 \lesssim n \lesssim 120$) low degree ($l \leq 4$) gravity modes (e.g. Balona et al. 1994; Kaye et al. 1999; Van Reeth et al. 2016; Saio et al. 2018b), which are useful for investigating the interior of stars since they have the highest mode energy in the near-core regions (Triana et al. 2015; Van Reeth et al. 2016). Shibahashi (1979) pointed out that the periods of high radial order g-modes ($n \gg l$) are equally spaced for chemically homogeneous non-rotating stars. Miglio et al. (2008) considered the effect of chemical composition gradients and found that dips or glitches appear in the period spacing patterns. Rotation also affects period spacings, causing the spacing of the prograde ($m > 0$) and zonal ($m = 0$) modes to decrease linearly with increasing period, and overall spacing to increase for the retrograde ($m < 0$) modes in the inertial reference frame (Bouabid et al. 2013; Ouazzani et al. 2017).

The long pulsation periods (~ 1 d), small period spacings (~ 1000 s) and the low pulsation amplitudes ($\sim 0.1\%$ variation) are challenging for ground-based observations. Thanks to the high precision and the long time-base of *Kepler* data (Borucki et al. 2010; Koch et al. 2010), period spacing patterns of tens of γ Dor stars have been detected. Some of these stars rotate slowly, hence nearly regular period spacings and rotation splittings are seen (e.g. Kurtz et al. 2014; Saio et al. 2015; Keen et al. 2015; Murphy et al. 2016; Li et al. 2019). However, most γ Dor stars rotate rapidly and the period spacings change significantly with period (e.g. Bedding et al. 2015; Van Reeth et al. 2015a; Saio et al. 2018b; Christophe et al. 2018). Besides g-modes, r-modes were also found in γ Dor stars by Van Reeth et al. (2016) and Saio et al. (2018a). The resolved r-modes generally show a quasi-linearly increasing period spacing with increasing period. However, the period spacing in r-modes drops at the larger period region (see the observation and theory in Saio et al. 2018a). Saio et al. (2018a) also explained observed power excesses in the periodogram as unresolved Rossby modes, in which the discrete frequencies are below the frequency resolution.

Here, we report 82 γ Dor stars in which the period spacing patterns of g-modes and r-modes are both seen. The co-existence of prograde and retrograde modes spacings breaks the correlation between the asymptotic spacing and the near-core rotation rate, and allows us to determine their values more precisely (Van Reeth et al. 2016). The

resolved r- and g-mode spacings also give many new possibilities for future research. They can be used in detailed asteroseismic modelling analyses (e.g. Aerts et al. 2018b) to study the inner physics of main-sequence stars, such as differential rotation and angular momentum transport (Aerts et al. 2018a; Van Reeth et al. 2018).

In Section 2, we briefly review the light curve reduction and pattern identification introduced by Li et al. (2019). In Section 3, we show how the traditional approximation of rotation (TAR) is used to model the observed patterns and reveals the near-core rotation rate. In Section 4, we report the observational results, such as the HR diagrams of our stars using *Gaia* data, the slope-period relations of g- and r-modes, near-core and surface rotation rates, and radial order distributions. Finally, we summarise our findings in Section 5.

2 PATTERN EXTRACTION

We used 4-year *Kepler* long-cadence (LC; 29.45-min sampling) light curves from the multi-scale MAP data pipeline (Stumpe et al. 2014). In each quarter, the light curve was divided by a second-order polynomial fit to remove any slow trend. We computed the Fourier transform and extracted the frequencies until the signal to noise ratio (S/N) was smaller than 3. The frequency uncertainty is given by

$$\sigma(f) = 0.44 \frac{\langle a \rangle}{a} \frac{1}{T}, \quad (1)$$

where $\langle a \rangle$ is the noise level in the amplitude spectrum, a is the amplitude of peak, and T is the total time span of the *Kepler* data ($T \simeq 1470$ d) (Montgomery & Odonoghue 1999; Kjeldsen 2003). Considering the S/N threshold, the frequency uncertainty in our work is smaller than 1×10^{-4} c/d.

Combination frequencies are seen in some γ Dor stars. They form several frequency groups in the power spectrum but the understanding of them is still an open question (Kurtz et al. 2015; Saio et al. 2018b). Likely combination frequencies were determined by the condition

$$|n_i f_i + n_j f_j - f_k| < 0.0002 \text{ c/d}, \quad (2)$$

where f_i and f_j are parent frequencies, n_i and n_j are the coefficients, and f_k is the combination candidate. We selected the 20 highest peaks as parent frequencies and set $|n_i| + |n_j| \leq 2$. In our work, the patterns dominated by the combination frequencies could be explained as the higher-degree prograde sectoral oscillations following Saio et al. (2018b).

A cross-correlation algorithm was implemented to detect the period spacing patterns between 0.2 d and 2 d (Li et al. 2019). We built a template to imitate the shape of periodogram, which was specified by the central peak's period P_c , the central peak's period spacing ΔP_c , the slope $\Sigma \equiv d\Delta P/dP$, and the number of peaks. The product of the template and the observed periodogram was used to measure the goodness of fit. The larger the product, the better the template described the observed pattern.

Then, the pattern is fitted by the formula

$$P_i = \Delta P_0 \frac{(1 + \Sigma)^i - 1}{\Sigma} + P_0 = \Delta P_0 (n' + \epsilon) \quad (3)$$

with the assumption that the period spacing changes linearly with period. Here, P_i is the i^{th} peak, P_0 is the first

peak, ΔP_0 is the first period spacing, Σ is the slope in the linear assumption, $n' \equiv \frac{(1+\Sigma)^{l-1}}{\Sigma}$ is the normalised index, and ϵ is the ratio $P_0/\Delta P_0$ (Li et al. 2019). Due to the occasional missing peaks, not all the period spacings can be calculated. This formula can be used to include isolated peaks, where there is no adjacent peak to calculate the period spacing value, and is helpful in calculating the radial order differences. Equation 3 also allows us to make an échelle diagram for less clear period spacing patterns and guide the pattern identification.

We can assign an angular degree l and an azimuthal order m to gravity modes. For the Rossby modes, the angular degree l is not defined and the value k is used instead (Lee & Saio 1997). For gravity modes, $k = l - |m|$. This paper adopts the convention that positive m represents the prograde modes while negative m represents retrograde modes.

2.1 An example: KIC 3240967

We present the period spacing patterns of KIC 3240967 as an example in Fig. 1. KIC 3240967 is the main-sequence γ Dor star with effective temperature of 7054 ± 80 K (Mathur et al. 2017). Its near-core rotation rate is 1.2857 ± 0.0008 d⁻¹ determined by the g- and r-modes pulsations (see section 3.2). Panel (a) of Fig. 1 shows the periodogram from 0.2 d to 2.4 d, where the vertical dashed lines show the best fit from Eq. 3 for each pattern. We found two period spacing patterns around 0.57 d and 0.95 d. The left pattern, marked by the blue dashed lines, comprises the dipole sectoral ($m = l = 1$) g-modes while the right one, marked by the black dashed lines, comprises the even ($k = -2$) retrograde ($m = -1$) r-modes (for the geometry of r-modes, please refer to the Fig.2 in Saio et al. (2018a)). The mode identifications are made based on the TAR fit in Section 3.2 and previous literature Van Reeth et al. (2018) and Saio et al. (2018a). Apart from these two patterns, the periodogram also displays two groups dominated by combination frequencies, located around 0.3 d and 1.5 d. The first is at twice the g-modes frequencies and the second is at the difference between the g and r-modes frequencies.

Panel (b) in Fig. 1 depicts the period spacing versus period. The period spacing for g-modes decreases from 500 s to 200 s with increasing period. For the r-mode pattern, the period spacing increases from 200 s to 1000 s with increasing period. Both patterns show deviations from the linear model, such as the dip at 0.92 d in the r-mode pattern, which is likely to be caused by the chemical composition gradient near the outer edge of the convective core (Miglio et al. 2008). The period spacing in the r-mode pattern also shows a drop at the longest period spacings (see the right side of Fig. 1 (h) for example), caused by the rapid change of the eigenvalue λ in the Laplace tidal equation (see Section 3 for example).

Panels (c) and (d) zoom in on the g-modes from panels (a) and (b), while panels (g) and (h) do the same for the r-modes. In Panels (e) and (i), the échelle diagrams are plotted sideways. The x-axis is the pulsation period while the y-axis is the term $P^{\text{obs}} - n'\Delta P$ from the fit of eq. 3. For the peaks that do not belong to the pattern, we plotted them at the location that minimised the value $P^{\text{obs}} - n'\Delta P$. Therefore, the y-axis reflects the deviations from the linear fit, similar to the curvature in the échelle diagram of solar-like oscillators

(e.g. Mazumdar et al. 2014). Panels (f) and (j) show the normalised sideways échelle diagram. The x-axis is the index of peaks, counting the first peak as 0, and the y-axis is the deviation over the local period spacing $(P^{\text{obs}} - n'\Delta P)/\Delta P$ expressed as a percentage.

3 NEAR CORE ROTATION

3.1 TAR fitting algorithm

We used the traditional approximation of rotation (TAR) to fit the period spacing patterns and derive the near-core rotation rate (Eckart 1960; Lee & Saio 1987; Townsend 2005). In the TAR, the θ -component of the rotation vector and the effects of the centrifugal force are ignored (Lee & Saio 1997). The TAR saves computational time and it provides a reliable approximation of the influence of rotation on the pulsation periods. Many stars have been investigated using the TAR to determine the near-core rotation rates (e.g. Van Reeth et al. 2016; Guo et al. 2017; Saio et al. 2018a,b) and we followed the method reported by Van Reeth et al. (2016). We also assumed that all the stars rotate rigidly, consistent with recent observations (e.g. Kurtz et al. 2014; Saio et al. 2015; Murphy et al. 2016; Schmid & Aerts 2016; Guo et al. 2017; Aerts et al. 2018a; Van Reeth et al. 2018).

The spin parameter is defined as

$$s \equiv \frac{2f_{\text{rot}}}{f_{\text{co}}}, \quad (4)$$

where f_{rot} is the rotation frequency and f_{co} is the pulsation frequency in the co-rotating frame. The spin parameter s represents the validity of the TAR. Ballot et al. (2012) showed that the TAR remains valid for the pulsation frequencies of gravito-inertial modes with $s < 1$, even in the case of large stellar rotation rates. This was further studied by Ouazzani et al. (2017). The authors found that the TAR is well suited for the analysis of prograde and zonal modes when the stellar rotation is less than 50% of the critical rotation rate, while retrograde gravito-inertial modes can be analysed with the TAR for rotation rates up to 25% of the critical rotation rate. However, the TAR has also been used to determine the near-core rotation rate in moderate-to fast-rotating stars, by fitting observed r-modes and prograde gravito-inertial modes, with satisfactory results (e.g., Saio et al. 2018b; Van Reeth et al. 2018).

The pulsation period in the co-rotating frame, given by the TAR, is

$$P_{nlm,\text{co}}^{\text{TAR}} = \frac{\Pi_0}{\sqrt{\lambda_{l,m,s}}} (n + \epsilon_g), \quad (5)$$

where Π_0 is the asymptotic period spacing, n is the radial order, the phase term ϵ_g is set as 0.5, and $\lambda_{l,m,s}$ is the eigenvalue of the Laplace tidal equation, which is specified by the angular degree l or the value k , the azimuthal order m and the spin parameter s .

Eq. 5 becomes the asymptotic relation (Shibahashi 1979) when $s \rightarrow 0$:

$$P_{nl} = \frac{\Pi_0}{\sqrt{l(l+1)}} (n + \epsilon_g). \quad (6)$$

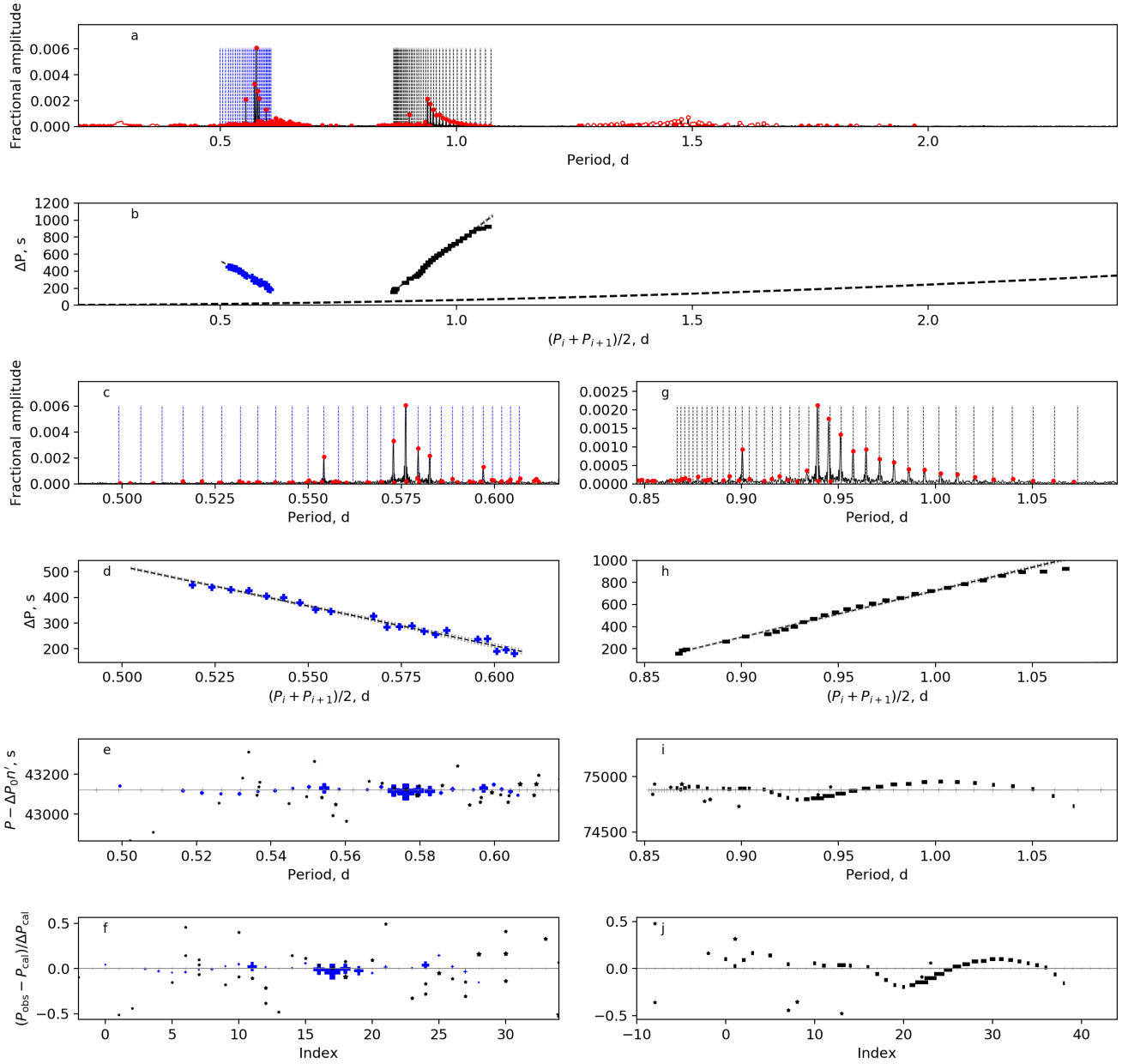


Figure 1. The g and r-mode patterns of KIC 3240967. Panel a: the amplitude spectrum with x-axis of period. The solid red circles present the detected independent frequencies while the open red circles show the combination frequencies. The vertical dashed lines are the linear fits for each pattern. The x-axis range is set from 0.2 d to 2.4 d for consistency for all stars. We found two independent frequency groups around 0.55 d and 0.95 d, and two combination frequency groups around 0.3 d and 1.5 d. There are two period spacing patterns. The blue one on the left is the $l = 1, m = 1$ g-modes while the black one on the right is the $k = -2, m = -1$ r-modes. Panel b: the period spacing patterns of KIC 3240967. The linear fits and uncertainties are shown by the black and grey dashed lines. The blue plus symbols are the g-modes and the black minus symbols are the r-modes. Panels c and d: the detail of the spectrum and period spacing pattern of g-modes. Panel e: the sideways échelle diagram of the g pattern. Panel f: the normalised sideways échelle diagram of the g-modes pattern. Panels g to j: same as (c – f) but for the r-mode patterns.

The period in the inertial frame is obtained by

$$P_{\text{in}}^{\text{TAR}} = \frac{1}{1/P_{\text{CO}}^{\text{TAR}} + m \cdot f_{\text{rot}}}. \quad (7)$$

The period spacing is calculated with equ. 5 and equ. 7 to be

$$\Delta P_{j,\text{in}}^{\text{TAR}} = P_{j+1,\text{in}}^{\text{TAR}} - P_{j,\text{in}}^{\text{TAR}}, \quad (8)$$

where j is the index sorted by the ascending period values. Note that the index j is not the radial order since the radial order for r-modes drops with increasing period in the inertial reference frame.

The TAR fit can only give the slope, rather than the exact locations of peaks. Hence we interpolated the period spacing $\Delta P_i^{\text{interp}}$ at the observational period P_i^{obs} using ΔP^{TAR}

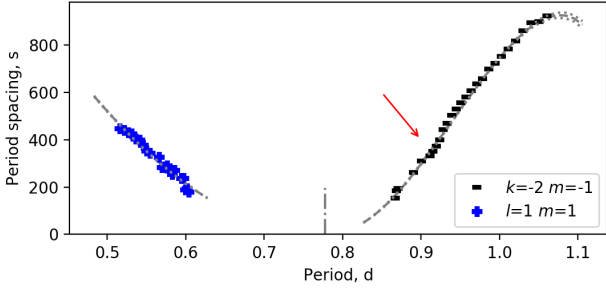


Figure 2. The TAR fit of KIC 3240967. The blue plus symbols show the $l = 1, m = 1$ gravity modes and the black minus symbols show the $k = -2, m = -1$ Rossby modes. The dashed grey curves display the best-fitted result. The error margins are plotted by the dotted lines, which are only visible at the right edge of the plot. The vertical dashed line denotes the fitted rotation period. The red arrow shows a dip.

and P^{TAR} . We defined the log likelihood function $\ln L$ as

$$\ln L \left(\Delta P | P^{\text{obs}}, \Pi_0, f_{\text{rot}}, k, m \right) = -\frac{1}{2} \sum_j \left[\frac{\Delta P_j^{\text{obs}} - \Delta P_j^{\text{interp}}}{\sigma_j^2} + \ln \left(2\pi\sigma_j^2 \right) \right], \quad (9)$$

where σ is the residual of the best fitting result. Since the observed patterns showed glitches and dips caused by the chemical composition gradient that the TAR does not take into account, and these variations are larger than the formal error margins on the pulsation periods, we used the residuals rather than the period spacing uncertainties to estimate the TAR model uncertainty. The data points below -1σ of the linear fit were excluded, because they were likely to be dips and mislead the fitting. We ran a Markov Chain Monte Carlo (MCMC) code to maximise the likelihood function Eq. 9 using the EMCEE package (Foreman-Mackey et al. 2013). The eigenvalue λ was given by GYRE (Townsend & Teitler 2013). The fit has two variables because the value k and the azimuthal order m were given based on the mode identification, so only the asymptotic spacing Π_0 and the near-core rotation rate f_{rot} were free parameters. The initial value of Π_0 was 4200 s, which is the most likely value of γ Dor stars from Van Reeth et al. (2016). The initial guess of f_{rot} was chosen to be halfway between the prograde g and retrograde r patterns because the period of the prograde mode in the inertial frame is smaller than the rotation period, and vice versa for the r-modes. The range of Π_0 was from 2000 to 20000 s to cover the typical range of both γ Dor and Slowly Pulsating B (SPB) stars. We searched for the best-fitting solution with a rotation rate f_{rot} between 0 and 5 d^{-1} . The upper limit of f_{rot} exceeds the critical rotation rate at which the centrifugal force causes a star to break apart. However, it is only selected to make sure that we can find a proper solution for every star. Based on our results (Fig. 11 shown in Section 4.6), there is no star which reaches this limit. We also set the radial orders from 5 to 150.

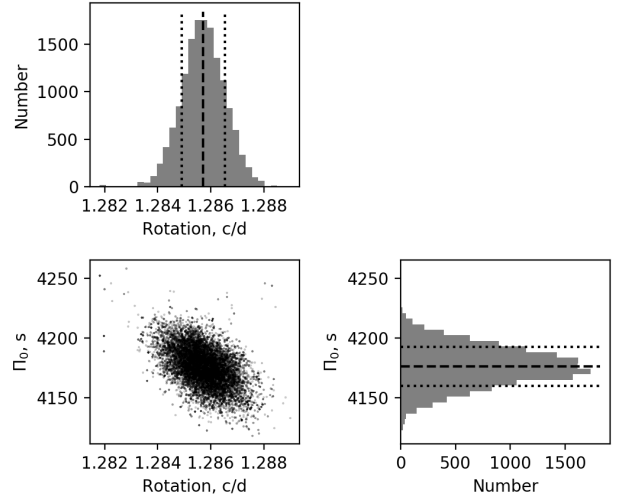


Figure 3. The posterior distributions for the TAR fit to KIC 3240967 using eq. 9. The dashed lines are the medians and the dotted lines show the $\pm 1\sigma$ areas.

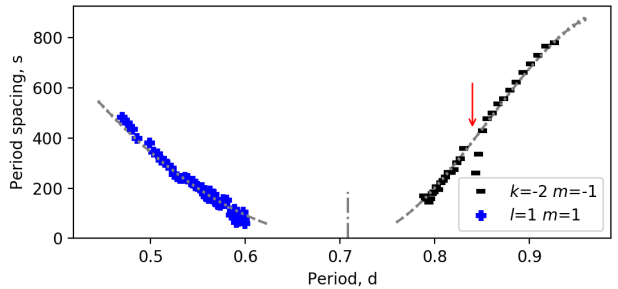


Figure 4. Same as Fig. 2 but for KIC 11775251. An obvious dip are seen in r-modes pattern at 0.85 d. Since the dip has been excluded, the fitting curves pass through other data points and do not be affected. The red arrow shows a dip.

3.2 TAR fitting of KIC 3240967

We again use KIC 3240967 to show how the TAR performed. Figure 2 gives the TAR fit result. The dashed curves that pass through the data points represent the best model, while the dotted lines are the $\pm 1\sigma$ region. We found that the model can explain the observational patterns. The observed period spacings of r-modes follow the TAR prediction and the slope changes very little with period except for a drop near the end of the r pattern, which is caused by the rapid change of the eigenvalue λ (see the Figure 1 of both Townsend 2003; Saio et al. 2018a). The theoretical slope of the g-mode period spacing pattern also changes with the period but only slightly. A dip in r-modes appears at $P \sim 0.91 \text{ d}$ (see the red arrow in Fig. 2), which might be the deviation from the asymptotic expression with the TAR, or is evidence of a chemical composition gradient effect (Miglio et al. 2008).

Figure 3 gives the posterior distributions of KIC 3240967. The best-fitting rotation rate is $f_{\text{rot}} = 1.2857 \pm 0.0008 \text{ d}^{-1}$ and the asymptotic spacing

is $\Pi_0 = 4180 \pm 20$ s. Because the prograde and retrograde modes co-exist, the correlation between f_{rot} and Π_0 is weak, so we have a better constraint on the near-core rotation.

Large dips are seen in some stars, for example, KIC 11775251, and were omitted from the TAR fit. Figure 4 shows the period spacing patterns and the TAR fit of KIC 11775251, in which a dip of r-modes is seen around ~ 0.85 d denoted by the red arrow. Since the dip has been removed, the fitting curves pass through other data points and are not affected. The fitting results are: $\Pi_0 = 4040 \pm 20$ s and $f_{\text{rot}} = 1.4115 \pm 0.0007 \text{ d}^{-1}$.

4 PERIOD SPACING PATTERNS OF 82 γ DOR STARS

We inspected the Fourier transforms of stellar light curves for 1593 *Kepler* targets with effective temperatures from 6600 K to 10000 K. Among these, we found 82 stars which show resolved period spacing patterns of both g-modes and r-modes. Table 1 shows mode identifications, observational pattern parameters, asymptotic spacings, near-core rotation rates, and the radial order ranges for our sample. The means of the periods are the average of all detected peaks. The mean period spacing is the slope of the linear fit between P_i and the index i , which is similar to the method used by White et al. (2011) to find p-mode frequency spacings ($\Delta\nu$) for solar-like oscillators. In Appendix A, we show the equivalent of Figs. 1 to 3 for all 82 stars with g and r-modes, sorted by rotation rate. The axes of panel (a) and (b) are the same for all figures, to make the comparison straightforward. Example diagrams are shown in figs A1 to A3. The figures for the other 81 stars are available as supplementary online material. Every star shows both downward and upward period spacing patterns, which are $l = 1, m = 1$ g-modes and $k = -2, m = -1$ r-modes, respectively. As the rotation decreases, both the g- and r-mode patterns move from left to right and the period gap between them increases. We also found 17 patterns which are identified as the $l = 2, m = 2$ g-modes (listed in Table 1). Only one star (KIC 5721632) has $k = -1, m = -1$ r-modes.

4.1 Stars on the HR diagram

Figure 5 shows the HR diagram of the 78 γ Dor stars (red circles) with clear r-mode patterns. 4 stars are excluded since their data quality are insufficient. Our exclusion conditions are: (1) the fractional parallax uncertainty is larger than 20%; (2) the star is 0.4 dex below the zero-age main-sequence (ZAMS); (3) there is no parallax or parallax error in *Gaia* DR2; (4) the star is identified as a binary. We took the effective temperatures T_{eff} from the latest version of the *Kepler* Stellar Properties Catalog (KSPC DR25, Mathur et al. 2017). The luminosity L was calculated by Murphy et al. (2019) using the *Gaia* Data Release 2 (DR2) parallax (Gaia Collaboration et al. 2016, 2018a,b,c). Murphy et al. (2019) compiled a catalogue of 1986 *Kepler* δ Scuti stars, which we added these to Fig. 5 as the grey dots. We also added the observational instability strip, defined by Murphy et al. (2019), based on the δ Sct pulsator fraction, shown in Fig. 5 as purple solid lines. The black solid lines represent the theoretical instability strip of γ Dor stars,

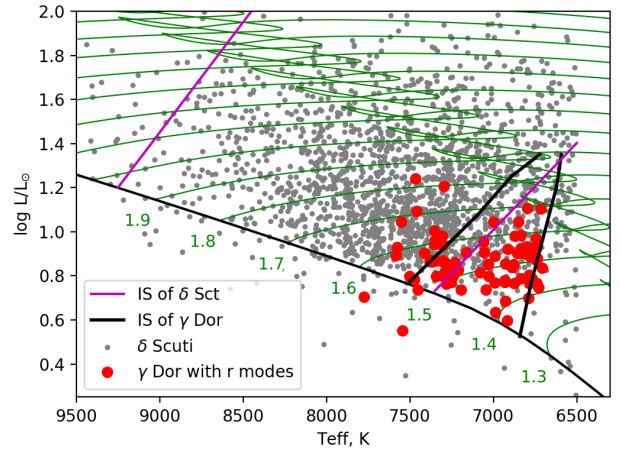


Figure 5. The δ Scuti and γ Doradus stars on the HR diagram. The grey dashed dots are the δ Scuti stars. The red circles are the 78 γ Dor stars with Rossby modes in this paper. The green numbers are the masses of the evolutionary tracks. The instability strips of δ Scuti and γ Dor are shown by the purple and black solid lines.

which was calculated by Dupret et al. (2005) and Bouabid et al. (2013). Our evolutionary tracks were computed in MESA (Paxton et al. 2011), v10108. Our ‘standard model’ at each mass had $X = 0.71$, $Z = 0.014$ (corresponding to $[M/H] = 0.036$), $\alpha_{\text{MLT}} = 1.8$, exponential core overshooting of 0.015 Hp , exponential H-burning shell over- and under-shooting of 0.015 Hp , exponential envelope overshooting of 0.025 Hp , diffusive mixing $\log D_{\text{mix}} = 0$ (in $\text{cm}^{-2}\text{s}^{-1}$), OPAL opacities, and the Asplund et al. (2009) solar abundance mixture. The parameters were chosen to be close to solar values, in agreement with observed metallicity values from spectroscopy and with the values from previously published asteroseismic modelling studies of g-mode pulsators (e.g. Schmid & Aerts 2016; Mombarg et al. 2019).

Figure 5 shows that most stars (both δ Scuti and γ Dor stars) are located above the zero-age main-sequence. δ Scuti stars show more spread than γ Dor stars and the latter generally have lower temperatures and lower luminosities. The distribution of γ Dor stars is wider than theoretically predicted, especially beyond the blue edge, which shows the inconsistency to the theoretical instability strip and challenges the current stellar model. However, the conclusions are still in debate since the uncertainty of T_{eff} is ~ 250 K. More accurate spectroscopic values for T_{eff} are required to confirm the location of the γ Dor instability strip. The effect of binarity also needs to be considered carefully.

The γ Dor stars in this paper are mostly confined to the low-luminosity region near the zero-age main-sequence (ZAMS). This makes sense, because r-modes are caused by rotation, which slows down with stellar evolution after the zero-age main-sequence. Young stars rotate faster and are more likely to exhibit r-modes in the detection region (0.2 to 2 d), hence we find more r-modes in stars near the ZAMS. We do not take the possibility of pre-main sequence γ Dor stars into account, although they were predicted by Bouabid et al. (2011). Another factor is that the low mass stars enter the γ Dor instability strip at the beginning of main sequence

Table 1. The mode identifications, mean pulsation periods, mean period spacings, slopes, asymptotic spacings, near-core rotation rates, and the minima and maxima of radial orders of 82 stars in this paper.

KIC	k	m	Mean P days	Mean ΔP Seconds	mean Σ days/days	Π_0 Seconds	f_{rot} d^{-1}	min n	max n
2575161	0	1	0.4	250	-0.0466 ± 0.0009	4470 ± 20	1.833 ± 0.001	21	55
	-2	-1	0.7	580	0.0753 ± 0.0004			9	28
2710594	0	1	0.7	360	-0.0290 ± 0.0003	4000 ± 10	0.9920 ± 0.0006	28	87
	-2	-1	1.2	470	0.0381 ± 0.0005			21	65
3240967	0	1	0.6	320	-0.0344 ± 0.0002	4180 ± 20	1.2857 ± 0.0008	31	59
	-2	-1	0.9	450	0.0507 ± 0.0004			14	52
3341457	0	1	0.4	120	-0.0292 ± 0.0007	3840 ± 40	1.859 ± 0.001	42	80
	-2	-1	0.6	100	0.0526 ± 0.0008			35	61
3445468	0	1	0.6	200	-0.0266 ± 0.0004	3860 ± 10	1.2037 ± 0.0007	36	102
	-2	-1	1.0	560	0.0377 ± 0.0006			17	43
3448365	0	1	0.7	330	-0.0301 ± 0.0008	4190 ± 10	1.0736 ± 0.0005	29	81
	-2	-1	1.1	380	0.0440 ± 0.0003			18	70
3449625	0	2	0.3	300	-0.0317 ± 0.0008	3970 ± 10	1.0514 ± 0.0005	25	48
	0	1	0.7	380	-0.0304 ± 0.0002			28	76
	-2	-1	1.1	310	0.049 ± 0.001			29	66
3626325	0	1	0.9	440	-0.0248 ± 0.0006	3910 ± 10	0.7820 ± 0.0005	46	82
	-2	-1	1.6	690	0.0203 ± 0.0006			23	54
3868382	0	2	0.4	360	-0.0325 ± 0.0002	4450 ± 10	0.8441 ± 0.0004	15	66
	0	1	0.7	630	-0.0320 ± 0.0003			21	69
	-2	-1	1.5	530	0.0358 ± 0.0002			19	63
3942392	0	2	0.2	120	-0.0402 ± 0.0006	4270 ± 30	1.627 ± 0.001	25	63
	0	1	0.5	230	-0.0383 ± 0.0003			27	64
	-2	-1	0.7	120	0.0511 ± 0.0005			34	63
3971170	0	1	0.7	190	-0.0264 ± 0.0007	3920 ± 30	1.198 ± 0.001	47	91
	-2	-1	1.0	240	0.066 ± 0.001			38	58
4069477	0	1	0.5	170	-0.0328 ± 0.0004	4020 ± 30	1.531 ± 0.002	40	74
	-2	-1	0.8	640	0.0532 ± 0.0006			13	26
4076350	0	2	0.3	160	-0.0583 ± 0.0008	3470 ± 20	1.248 ± 0.001	39	57
	0	1	0.6	230	-0.0454 ± 0.0008			47	78
	-2	-1	1.0	430	0.0412 ± 0.0007			20	54
4077558	0	1	0.6	260	-0.0340 ± 0.0001	3960 ± 10	1.2063 ± 0.0008	30	87
	-2	-1	1.1	620	0.0409 ± 0.0006			13	40
4261149	0	1	0.7	220	-0.0209 ± 0.0009	4820 ± 40	1.1251 ± 0.0009	45	83
	-2	-1	1.1	440	0.024 ± 0.004			27	38
4448157	0	1	0.6	260	-0.0303 ± 0.0003	4000 ± 20	1.1698 ± 0.0008	33	85
	-2	-1	1.0	200	0.0461 ± 0.0007			37	69
4566474	0	1	0.6	280	-0.0312 ± 0.0006	4130 ± 10	1.2345 ± 0.0007	30	77
	-2	-1	1.0	570	0.0435 ± 0.0004			15	42
4585982	0	1	0.6	180	-0.0249 ± 0.0003	3370 ± 20	1.3924 ± 0.0009	40	97
	-2	-1	0.8	130	0.030 ± 0.001			41	88
4672176	0	1	0.4	200	-0.0398 ± 0.0005	4280 ± 20	1.748 ± 0.001	25	68
	-2	-1	0.7	290	0.0723 ± 0.0004			11	47
4758316	0	1	0.6	380	-0.0395 ± 0.0004	4470 ± 20	1.2445 ± 0.0009	24	62
	-2	-1	1.0	820	0.042 ± 0.001			13	24
4774208	0	1	0.4	190	-0.0427 ± 0.0005	4340 ± 20	1.834 ± 0.001	30	58
	-2	-1	0.6	290	0.0751 ± 0.0004			11	45
4843037	0	1	0.5	180	-0.0320 ± 0.0003	3910 ± 20	1.627 ± 0.001	32	75
	-2	-1	0.7	330	0.0604 ± 0.0004			13	52
4857064	0	1	1.1	570	-0.0206 ± 0.0002	3832 ± 9	0.5738 ± 0.0004	40	103
	-2	-1	2.3	740	0.010 ± 0.001			38	61
4859790	0	1	0.5	240	-0.0358 ± 0.0004	4550 ± 20	1.4584 ± 0.0007	29	65
	-2	-1	0.8	320	0.0611 ± 0.0004			11	61
5040435	0	1	0.5	190	-0.0296 ± 0.0004	4070 ± 30	1.440 ± 0.001	35	78
	-2	-1	0.8	280	0.073 ± 0.004			30	41
5114382	0	1	0.7	230	-0.0234 ± 0.0002	4110 ± 30	1.140 ± 0.001	47	82
	-2	-1	1.1	510	0.057 ± 0.002			22	44
5294571	0	2	0.2	100	-0.0318 ± 0.0004	4150 ± 20	1.6421 ± 0.0009	36	63
	0	1	0.5	200	-0.0383 ± 0.0005			32	63
	-2	-1	0.7	250	0.0620 ± 0.0004			17	54
5391059	0	1	0.4	190	-0.0419 ± 0.0004	4210 ± 20	1.796 ± 0.001	29	60
	-2	-1	0.7	340	0.0710 ± 0.0002			12	42
5476854	0	1	1.0	410	-0.0183 ± 0.0004	4060 ± 10	0.6647 ± 0.0004	55	93
	-2	-1	1.9	630	0.0281 ± 0.0006			31	66

Table 1. continued.

KIC	k	m	Mean P days	Mean ΔP Seconds	mean Σ days/days	Π_0 Seconds	f_{rot} d^{-1}	min n	max n
5640438	0	1	0.7	370	-0.0276 ± 0.0003	4230 ± 20	0.9788 ± 0.0005	36	74
	-2	-1	1.2	390	0.0376 ± 0.0003			15	82
5706866	0	1	0.6	180	-0.027 ± 0.001	3610 ± 20	1.218 ± 0.001	61	91
	-2	-1	1.1	610	0.0342 ± 0.0004			16	38
5708550	0	1	0.9	360	-0.0233 ± 0.0004	3840 ± 10	0.7911 ± 0.0006	41	100
	-2	-1	1.7	800	0.010 ± 0.001			17	41
5721632	0	1	0.4	320	-0.0479 ± 0.0005	4371 ± 8	1.6969 ± 0.0009	18	54
	-2	-1	0.7	220	0.0696 ± 0.0004			25	44
	-1	-1	1.9	4270	0.094 ± 0.001			25	43
5801556	0	2	0.3	230	-0.0401 ± 0.0008	4240 ± 20	1.2186 ± 0.0008	20	56
	0	1	0.6	230	-0.042 ± 0.002			44	70
	-2	-1	1.1	740	0.0335 ± 0.0006			13	30
5984615	0	1	0.8	240	-0.0235 ± 0.0002	3820 ± 20	0.9892 ± 0.0007	48	102
	-2	-1	1.3	530	0.0368 ± 0.0008			21	62
6048255	0	1	0.6	170	-0.0252 ± 0.0002	3750 ± 30	1.3748 ± 0.0009	44	95
	-2	-1	0.8	130	0.0374 ± 0.0005			41	77
6291473	0	2	0.2	110	-0.0329 ± 0.0004	5770 ± 40	1.671 ± 0.001	21	64
	0	1	0.5	210	-0.0342 ± 0.0004			27	58
	-2	-1	0.7	310	0.11 ± 0.02			23	30
6301745	0	1	0.3	210	-0.0495 ± 0.0007	4210 ± 40	2.297 ± 0.002	23	43
	-2	-1	0.5	110	0.0672 ± 0.0008			23	48
6468987	0	1	0.5	230	-0.035 ± 0.001	4020 ± 50	1.551 ± 0.002	30	65
	-2	-1	0.7	190	0.07 ± 0.01			38	46
6696689	0	1	0.7	180	-0.0239 ± 0.0002	3830 ± 20	1.1057 ± 0.0006	52	105
	-2	-1	1.0	190	0.0347 ± 0.0003			45	80
6806005	0	1	0.6	240	-0.0307 ± 0.0006	4000 ± 20	1.3235 ± 0.0008	35	72
	-2	-1	0.9	380	0.0501 ± 0.0004			14	61
6923424	0	2	0.2	80	-0.0398 ± 0.0005	4230 ± 30	2.023 ± 0.002	23	75
	0	1	0.4	240	-0.0496 ± 0.0006			17	56
	-2	-1	0.5	80	0.0494 ± 0.0006			32	60
7039007	0	1	0.7	290	-0.0300 ± 0.0005	3970 ± 20	1.039 ± 0.001	46	75
	-2	-1	1.2	650	0.0257 ± 0.0007			21	36
7137351	0	1	0.6	230	-0.0329 ± 0.0003	3820 ± 10	1.2129 ± 0.0009	36	89
	-2	-1	1.0	550	0.0353 ± 0.0003			16	48
7436266	0	1	0.6	220	-0.0298 ± 0.0003	4070 ± 10	1.2897 ± 0.0007	32	91
	-2	-1	0.9	370	0.0487 ± 0.0006			10	68
7538181	0	1	0.6	260	-0.0335 ± 0.0008	3840 ± 20	1.1939 ± 0.0009	41	73
	-2	-1	1.1	580	0.0405 ± 0.0009			14	41
7551589	0	1	0.6	180	-0.0292 ± 0.0003	3820 ± 20	1.3182 ± 0.0009	43	91
	-2	-1	0.9	490	0.0460 ± 0.0008			15	46
7583663	0	1	0.6	280	-0.0307 ± 0.0005	4220 ± 20	1.1608 ± 0.0007	38	71
	-2	-1	1.0	180	0.0385 ± 0.0005			39	70
7596250	0	1	0.6	350	-0.0346 ± 0.0005	4290 ± 20	1.1876 ± 0.0007	28	67
	-2	-1	1.0	590	0.0502 ± 0.0006			17	38
7621649	0	1	0.8	510	-0.0270 ± 0.0002	3990 ± 10	0.7745 ± 0.0004	31	81
	-2	-1	1.6	530	0.0307 ± 0.0004			29	63
7778826	0	1	0.4	270	-0.0510 ± 0.0004	4020 ± 30	2.060 ± 0.002	21	48
	-2	-1	0.6	330	0.0792 ± 0.0007			9	41
8198031	0	1	0.4	170	-0.0375 ± 0.0005	4140 ± 20	1.855 ± 0.001	26	75
	-2	-1	0.6	370	0.0767 ± 0.0006			13	39
8263970	0	1	0.4	170	-0.0393 ± 0.0007	4180 ± 20	1.946 ± 0.001	22	77
	-2	-1	0.6	470	0.0786 ± 0.0001			11	30
8316105	0	1	0.6	300	-0.0354 ± 0.0005	4240 ± 20	1.3352 ± 0.0008	25	71
	-2	-1	0.9	420	0.0539 ± 0.0004			16	51
8330056	0	1	0.4	170	-0.0393 ± 0.0005	4100 ± 20	1.913 ± 0.001	27	69
	-2	-1	0.6	390	0.0731 ± 0.0006			10	43
8351778	0	2	0.3	260	-0.0361 ± 0.0007	3760 ± 20	0.9645 ± 0.0009	30	58
	0	1	0.7	320	-0.0262 ± 0.0002			41	85
	-2	-1	1.2	130	0.026 ± 0.002			72	86
8375138	0	1	0.5	200	-0.0376 ± 0.0003	4150 ± 20	1.6421 ± 0.0009	30	66
	-2	-1	0.7	400	0.0659 ± 0.0003			9	43
8973529	0	2	0.3	140	-0.0308 ± 0.0003	4000 ± 20	1.204 ± 0.001	23	91
	0	1	0.6	320	-0.0325 ± 0.0004			23	84
	-2	-1	0.9	220	0.066 ± 0.002			39	60

Table 1. continued.

KIC	k	m	Mean P days	Mean ΔP Seconds	mean Σ days/days	Π_0 Seconds	f_{rot} d^{-1}	min n	max n
9210943	0	1	0.4	300	-0.043 ± 0.001	4310 ± 20	1.703 ± 0.001	25	46
	-2	-1	0.7	410	0.0693 ± 0.0005			10	41
9419182	0	2	0.3	180	-0.0385 ± 0.0006	4190 ± 10	1.1510 ± 0.0006	28	63
	0	1	0.7	250	-0.0282 ± 0.0003			38	83
	-2	-1	1.1	470	0.0434 ± 0.0006			16	62
9480469	0	1	0.5	160	-0.032 ± 0.001	4330 ± 20	1.554 ± 0.001	41	73
	-2	-1	0.8	400	0.0647 ± 0.0002			12	45
9594007	0	2	0.2	130	-0.0428 ± 0.0005	3980 ± 20	1.671 ± 0.001	28	54
	0	1	0.5	200	-0.0366 ± 0.0008			23	81
	-2	-1	0.7	160	0.0550 ± 0.0007			26	62
9594100	0	2	0.3	240	-0.0370 ± 0.0005	4110 ± 20	1.2159 ± 0.0009	24	48
	0	1	0.6	260	-0.0313 ± 0.0003			32	78
	-2	-1	1.0	320	0.03 ± 0.01			32	47
9652302	0	1	0.8	330	-0.021 ± 0.001	3710 ± 20	0.9147 ± 0.0006	49	89
	-2	-1	1.3	270	0.061 ± 0.003			48	67
9716563	0	2	0.4	210	-0.0258 ± 0.0002	3860 ± 10	0.9081 ± 0.0008	30	84
	0	1	0.7	570	-0.0307 ± 0.0003			24	68
	-2	-1	1.5	820	0.0119 ± 0.0007			18	27
9962653	0	1	0.4	200	-0.0410 ± 0.0004	4150 ± 20	1.763 ± 0.001	28	62
	-2	-1	0.7	290	0.0686 ± 0.0002			11	50
10423501	0	1	0.8	480	-0.0271 ± 0.0002	4240 ± 20	0.8420 ± 0.0006	30	77
	-2	-1	1.4	480	0.0339 ± 0.0009			37	51
10481462	0	1	0.4	210	-0.052 ± 0.001	4410 ± 30	2.208 ± 0.002	18	53
	-2	-1	0.5	440	0.0973 ± 0.0005			11	26
10818266	0	1	0.4	250	-0.0468 ± 0.0005	4290 ± 20	1.849 ± 0.001	19	57
	-2	-1	0.7	460	0.0772 ± 0.0003			11	34
10859386	0	1	0.4	290	-0.045 ± 0.001	4420 ± 30	1.813 ± 0.001	24	45
	-2	-1	0.6	120	0.062 ± 0.002			35	52
11256244	0	1	0.8	300	-0.0242 ± 0.0002	3930 ± 10	0.9622 ± 0.0006	46	85
	-2	-1	1.3	640	0.026 ± 0.001			23	45
11466960	0	1	0.6	210	-0.0324 ± 0.0005	4240 ± 10	1.3874 ± 0.0007	30	83
	-2	-1	0.9	400	0.0560 ± 0.0004			13	53
11519475	0	1	0.5	190	-0.0333 ± 0.0003	4070 ± 30	1.576 ± 0.001	30	76
	-2	-1	0.7	200	0.0550 ± 0.0008			31	50
11550154	0	2	0.2	90	-0.0409 ± 0.0003	4140 ± 20	2.017 ± 0.001	25	59
	0	1	0.4	140	-0.0367 ± 0.0006			24	80
	-2	-1	0.6	320	0.0794 ± 0.0005			11	40
11571757	0	2	0.4	220	-0.048 ± 0.002	6130 ± 30	1.0291 ± 0.0005	29	52
	0	1	0.8	240	-0.0223 ± 0.0004			32	105
	-2	-1	1.1	380	0.064 ± 0.002			26	46
11657371	0	1	0.4	250	-0.0436 ± 0.0007	3900 ± 40	1.848 ± 0.002	27	52
	-2	-1	0.6	60	0.077 ± 0.002			50	71
11775251	0	1	0.6	190	-0.0327 ± 0.0003	4040 ± 20	1.4115 ± 0.0007	32	89
	-2	-1	0.8	350	0.0572 ± 0.0006			15	49
11907454	0	1	0.6	240	-0.0368 ± 0.0006	4200 ± 20	1.3387 ± 0.0006	31	75
	-2	-1	0.9	270	0.0543 ± 0.0001			11	67
12066947	0	1	0.4	140	-0.0399 ± 0.0009	4170 ± 30	2.159 ± 0.002	26	65
	-2	-1	0.5	270	0.0804 ± 0.0005			12	45
12170722	0	2	0.2	100	-0.0362 ± 0.0004	4270 ± 20	1.702 ± 0.001	23	78
	0	1	0.5	150	-0.0334 ± 0.0002			34	80
	-2	-1	0.7	390	0.0715 ± 0.0005			11	39
12303838	0	1	0.6	250	-0.0329 ± 0.0004	4160 ± 20	1.3301 ± 0.0007	34	71
	-2	-1	0.8	190	0.0483 ± 0.0005			28	69
12520187	0	1	0.4	310	-0.0568 ± 0.0006	4650 ± 50	1.872 ± 0.002	19	45
	-2	-1	0.6	90	0.062 ± 0.003			30	52

and stay in it longer than high mass stars. Hence they are more likely to be observed. This also explains why γ Dor stars generally show smaller T_{eff} and $\log L$.

4.2 Period spacings

Our sample is large enough to show some general features for the g and r-modes of γ Dor stars. The periodograms of r and g-mode stars show two main groups of modes. At shorter periods are the $l = 1, m = 1$ g-modes and at longer periods are the $k = -2, m = -1$ r-modes. Although the asymptotic

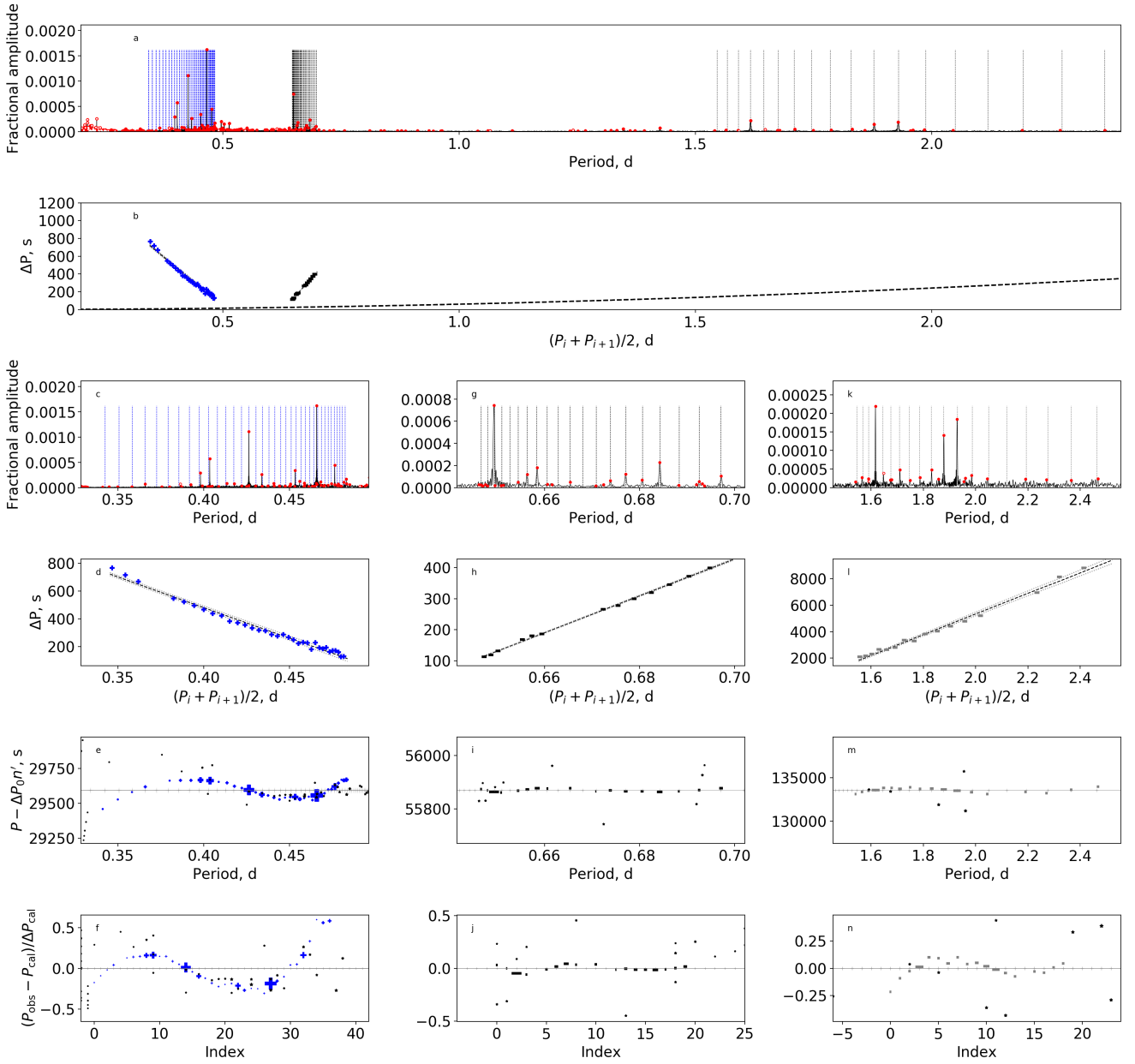


Figure 6. Period spacings and the sideways échelle diagrams of KIC 5721632. Panels (k) to (n) show the $k = -1, m = -1$ r-modes pattern. The period spacings are too larged to display in panel (b).

spacing Π_0 of γ Dor is typically around 4200 s (Van Reeth et al. 2016), the period spacings vary greatly due to the rapid rotation, from a few hundred seconds to 1000 s, but in each star, it is similar among both the g and r-modes. The period spacings of g-modes decrease quasi-linearly with period, which is the rotational effect for prograde g-modes (Bouabid et al. 2013; Ouazzani et al. 2017). However, the period spacings of r-modes increase linearly with periods, and sometimes show a drop at the long-period end (see e.g. Fig. 1 (h) and Saio et al. 2018a).

We found that almost all the r-modes have the quantum numbers of $k = -2, m = -1$, although other numbers were also reported by Saio et al. (2018a). The reason is likely that the

period spacing of $k = -2, m = -1$ modes is easily detected in *Kepler* data, compared to tens of seconds of $k = -2, m = -2$ modes or several thousands of seconds of $k = -1, m = -1$ modes. Also, $k = -2, m = -2$ modes generally have larger amplitudes (Saio et al. 2018a).

KIC 5721632 is the only star which shows convincing $k = -1, m = -1$ r-modes. Figure 6 shows its amplitude periodogram, period spacing patterns and the échelle diagram. The rotation rate is $f_{\text{rot}} = 1.6969 \pm 0.0009 \text{ d}^{-1}$ and the asymptotic spacing is $\Pi_0 = 4371 \pm 8 \text{ s}$, as shown in Figs 7 and 8. In the lower-left panel of Fig. 8, the asymptotic spacing negatively correlates with the rotation rate, since the fitting is dominated by the retrograde $k = -1, m = -1$ r-modes.

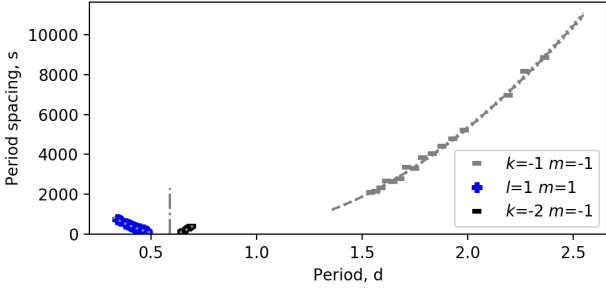


Figure 7. The TAR fit of KIC 5721632.

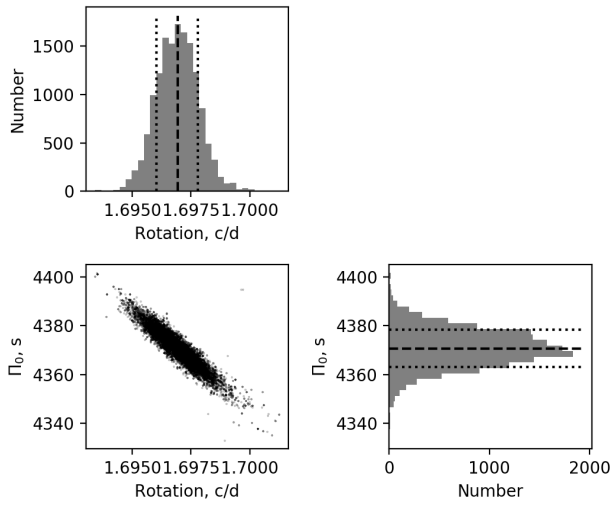


Figure 8. The posterior distributions of KIC 5721632. The best model has $\Pi_0 = 4371 \pm 8$ s and $f_{\text{rot}} = 1.6969 \pm 0.0009$ d $^{-1}$. The fitting is dominated by the retrograde $k = -1, m = -1$ r-modes, hence Π_0 shows a negative correlation with f_{rot} in the lower-left panel.

The period spacing of the $k = -1, m = -1$ pattern keeps increasing from 2000 s to 8000 s, showing different feature from $k = -2, m = -1$ Rossby modes. We also noticed that there are two stars, KIC 5721610 and KIC 5721628, which are close to KIC 5721632 on the sky within 6 arcseconds. We evaluated the light curve of KIC 5721632 for contamination from those two stars. The power spectra of those two stars were calculated and we do not find any g- or r-mode oscillations. So the light curve of KIC 5721632 was not contaminated and the $k = -1, m = -1$ Rossby modes are most likely real.

4.3 Asymmetric amplitude envelopes

Saio et al. (2018a) used the visibility over the square root of kinetic energy ($\text{Vis.}/\sqrt{\text{K.E.}}$) to calculate the amplitude of r-modes. They showed that the $k = -2, m = -1$ modes have the highest amplitudes compared to other r-modes and the amplitude envelope is strongly asymmetric, with a steep low-period side. The relatively large amplitude is helpful to identify the $k = -2, m = -1$ r-modes. We also observed the asymmetric amplitude envelope in some stars, e.g. Fig. 1

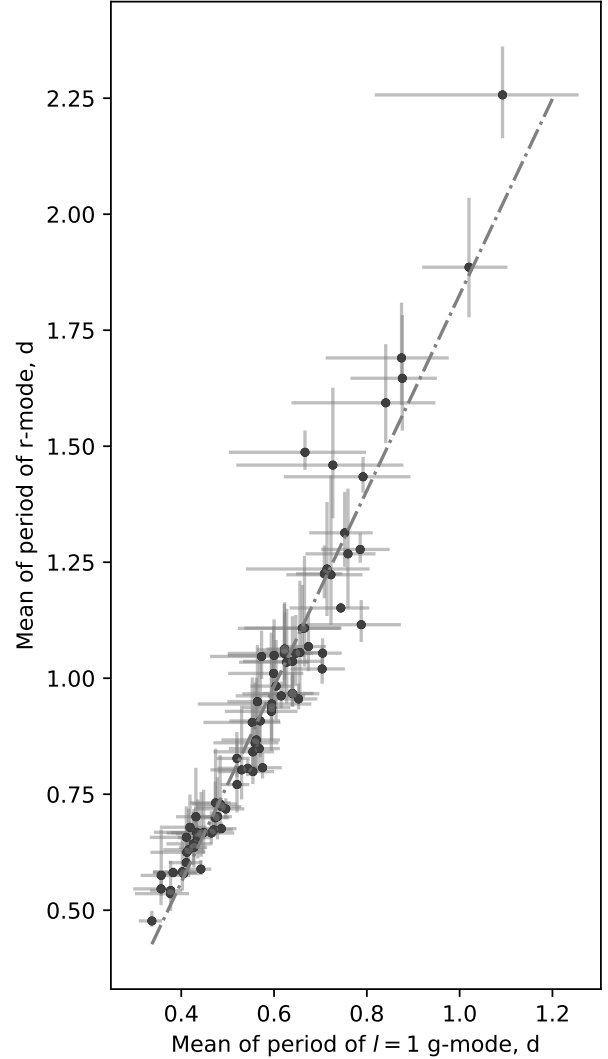


Figure 9. The mean period relation between the $l = 1, m = 1$ g-mode patterns and the $k = -2, m = -1$ r-mode patterns. The black dots show the means of the periods in each pattern. Since the period spacing changes, the means of the periods are not in the centre. The grey solid lines are the period ranges. The dashed-dotted line is the linear fit.

(g), where the amplitude increases rapidly at $P \sim 0.94$ d and drops slowly after that. However, it shows a lot of small peaks and several strong peaks before the predicted amplitude rise. For some other stars, the r-mode patterns do not show the predicted amplitude envelope, e.g. Fig. 6 (g). A more complete theory may be needed to address this observation.

4.4 Periods of Rossby modes

Figure 9 shows the period relation between the $l = 1, m = 1$ g-modes and $k = -2, m = -1$ r-modes. The black points are the means of the periods of each pattern, which are the averaged value of all the detected periods. Since the period spacing changes with period, the means of periods are not the centre

of patterns. The grey lines are not error bars, they show the period ranges of g- and r-modes, respectively. We found that the means of the periods of g- and r-modes are related by a linear fit with

$$\langle P_r \rangle = (2.06 \pm 0.05) \langle P_g \rangle - (0.25 \pm 0.03) \text{ d}, \quad (10)$$

where $\langle P_r \rangle$ is the means of the periods of r-modes and $\langle P_g \rangle$ is the one of g-modes. The linear fit has the slope 2.06 ± 0.05 and the intercept is -0.25 ± 0.03 d, shown as the grey dashed line. Since the means of periods must be located within the period ranges, to calculate the uncertainties of the linear fit, we used the period ranges as 3σ to make perturbations of the data.

Based on the slope and the small intercept, we conclude the r-mode periods are close to twice the g-mode periods. The relationship helps guide a search for the r-modes in more stars, if the amplitudes of r-mode are not obvious.

4.5 Slope–period relation

Figure 10 shows the slope versus period relation of 82 γ Dor stars. The x-axis is the mean of the periods, which is the same as shown in Fig. 9. The y-axis is the slope assuming the period spacing changes quasi-linearly with the period, fitted by Eq. 3. Different markers and colours stand for different modes. The points cluster into several groups and display different trends based on their quantum numbers. For the $l = 1, m = 1$ g-modes (blue triangles), the slopes are negative and increase towards zero with the mean period, with a large spread. The points of the $l = 2, m = 2$ g-modes (green stars) lie on the left of the dipole g-modes with similar slopes. Finally, the slopes of r-mode patterns (red circles) are larger than zero, and show a clear decreasing trend with the mean period.

To compare these results with theory, we calculated period spacing patterns from the TAR. The range of Π_0 was 3600 to 5600 s with step of 200 s, and f_{rot} ranged from 0 to 4 d^{-1} . For r modes, we averaged over overtones with $10 \leq n \leq 30$. Results are shown as red lines in Fig. 10, with less transparency corresponding to larger Π_0 . Considering the mean of periods and slope change with the radial order region for the g-modes, we measured the slope of calculated patterns in two regions: $10 \leq n \leq 30$ and $30 \leq n \leq 50$, showing these as blue and cyan lines in Fig. 10. Each solid line in Fig. 10 has the same Π_0 and the same n region along its length, but the rotation rate increases from right to left. We use the darker lines to represent larger Π_0 . The lighter the curve is, the smaller its Π_0 is.

From the calculated curves, we find that if we want to cover the g-mode observational points, curves that span different n are needed. However, the features of different radial orders differ dramatically. The blue curves with n from 10 to 30 generally show smaller mean periods and steeper slopes (reaching -0.09 when the mean period is at 0.2 d). The cyan curves with radial order from 30 to 50 have larger mean periods and their slopes only reach -0.05 when the mean period arrives at 0.2 d. They show an overlapping area between 0.4 d and 0.6 d.

For the r-modes, the period spacing decreases at the long periods due to the rapid change of the eigenvalue λ . This affects the calculated slope value but is not common in the observations, so we only adopted the periods before

the spacing drop, which is caused by the rapid change of the eigenvalue λ (see Fig. 2). Only the results with $10 \leq n \leq 30$ and $0.7 \text{ d}^{-1} \leq f_{\text{rot}} \leq 4 \text{ d}^{-1}$ were used, since this parameter space covered the observations well (red lines in Fig. 10). The radial order range from 10 to 30 of r-modes can explain the observational data. The correlation between the slope and the mean period spacing is caused by the rotation rate. The more rapidly the star rotates, the shorter the mean period and the larger the slope. In Fig. 10, we marked six outliers, which are caused by the systematic influence of dips in the pattern. The measurement of the slope is affected strongly by the intrinsic dips or fluctuations, which reflects the limit of the linear assumption in Eq. 3.

Figure 10 also shows the calculated relationships between the slope and mean period (as a function of rotation), for several discrete values of asymptotic spacing Π_0 . It can guide the pattern identification for other γ Dor stars. If a period spacing pattern does not follow the relation, several possibilities should be considered: the pattern includes a partly-observed dip (e.g. Li et al. 2019); the star is an SPB star, which generally has larger Π_0 and steeper slope (Pápics et al. 2017); the period spacing identification is misled by missing peaks.

4.6 Asymptotic spacing and rotation

The TAR fit gives the near-core rotation rate f_{rot} and the asymptotic spacing Π_0 for every star. Figure 11 shows the distributions and correlation for these two parameters. The uncertainties of the histograms are square roots of the histogram heights, assuming they are Poisson-distributed. Most stars have asymptotic spacings between 3600 and 4500 s (Fig. 11 (a)), which is consistent with Van Reeth et al. (2016). The asymptotic spacing decreases with evolution, hence is considered as an indicator of stellar age. However, it is also affected by other physical parameters, such as metallicity, mixing length and convective core overshooting. Figure 11 (c) is the distribution of the rotation rate f_{rot} . The slowest rotator is KIC 4857064 with $f_{\text{rot}} = 0.5738 \pm 0.0004 \text{ d}^{-1}$ and the fastest one is KIC 6301745 with $f_{\text{rot}} = 2.297 \pm 0.002 \text{ d}^{-1}$. Most stars rotate between 1 and 2 d^{-1} , much faster than the Sun but typical for A to F stars (Royer et al. 2007).

Figure 11 (b) displays the lack of correlation between Π_0 and f_{rot} . Most stars have the asymptotic spacings around 4000 s and the rotation rates from 1 to 2 d^{-1} , showing typical ranges for γ Dor stars. We found two outliers: KIC 11571757, and KIC 6291473, whose period spacing patterns are seen in the online supplementary material. The asymptotic spacings of KIC 11571757 and KIC 6291473 are 6130 ± 30 s and 5770 ± 40 s, respectively. These are obviously higher than the range of γ Dor stars but are typical of SPB stars (5600 to 15400 s, see Pápics et al. 2017). However, their effective temperatures are too low to be B-type stars. These two stars may be at the beginning of the main sequence hence show large asymptotic spacings, or the identifications of period spacing patterns are misled by missing peaks.

We also notice that a gap at $f_{\text{rot}} \sim 1.5 \text{ d}^{-1}$ separates the data points into two groups. The f_{rot} distribution in Fig. 11 (c) show two peaks around 1.2 d^{-1} and 1.8 d^{-1} . We tried several different bins and the gap is still apparent. Whether it is

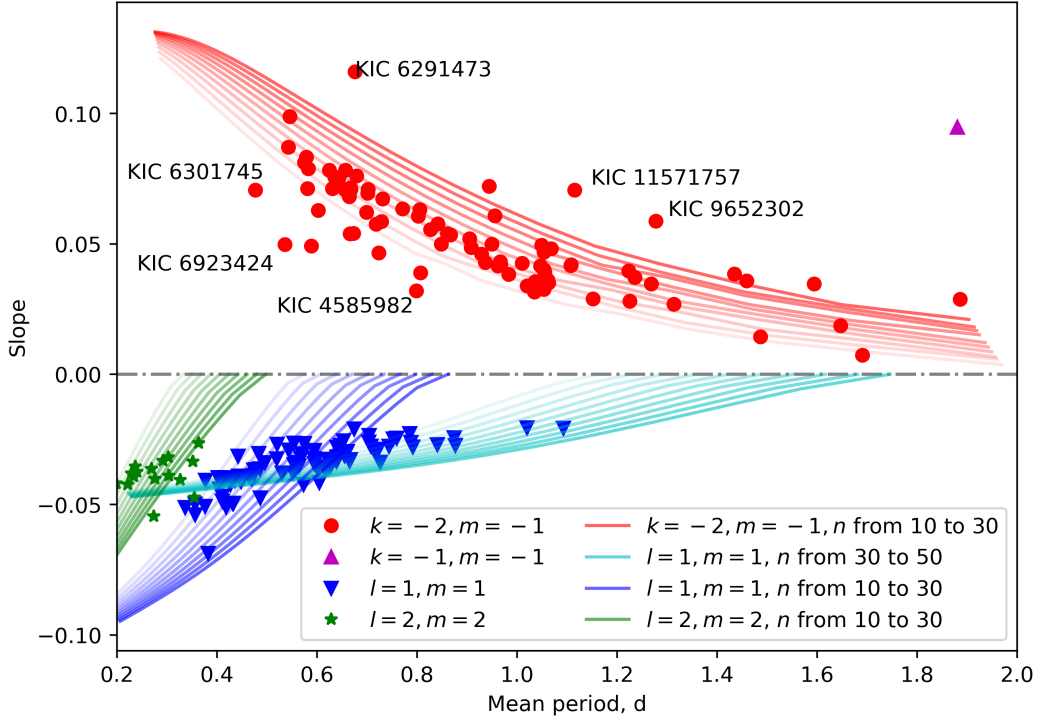


Figure 10. The slope–period relation with theoretical curves for r-modes (positive slopes) and g-modes (negative slopes). We calculated the theoretical period spacing slopes in two radial order regions: 10 to 30 and 30 to 50, respectively. A given curve has the same Π_0 and n region but the rotation rate increases from right to left. The transparencies of curves represent the Π_0 , which is from 360 s to 5400 s with step of 200 s. The lighter, the smaller the Π_0 is. Curves with different colours have different radial order ranges and different quantum numbers.

a real effect or caused by the limited numbers of the sample is still an open question.

We do not find any strong correlation between Π_0 or f_{rot} and T_{eff} , which is colour-coded in Fig. 11. Both rotation and Π_0 are expected to decrease with evolution and effective temperature, but the processes are presumably affected by many other parameters, such as the initial rotation rate, the mechanism of angular momentum transfer, or extra diffusion. It seems that 82 stars are still too few to reveal a correlation. As shown in Fig. 5, most stars in our sample are close to the ZAMS. The range of stellar ages in our sample may also be not long enough to show the correlation from the evolutionary effect. Also, more precise values of effective temperatures are still needed to confirm the theoretical prediction.

4.7 Rotation from core to surface

The rotation profile from the core to the surface is the key to understand the angular momentum transport and chemical mixing processes. As pointed out in Section 4.6, the g- and r-mode period spacings are used to constrain near-core rotation rates inside the stars. Several methods give the opportunity to measure the rotation of the outer stellar envelope, such as p-mode splittings (e.g. Kurtz et al. 2014; Saio et al. 2015; Schmid & Aerts 2016), projected rotation velocity ($v \sin i$) (e.g. Murphy et al. 2016), rotational spot modulation (e.g. Degroote et al. 2011; McQuillan et al.

Table 2. The surface modulation of 6 γ Dor tars. ‘EB’ means the star is a binary from Kirk et al. (2016). ‘SPOT’ means the surface modulation is caused by spots. $f_{\text{rot},i}$ is the near-core rotation rate fitted by g- and r-mode period spacing patterns. $f_{\text{rot},o}$ is the surface rotation rate from spot modulation.

KIC	Type	$f_{\text{rot},i}$, d^{-1}	$f_{\text{rot},o}$, d^{-1}	$f_{\text{rot},i}/f_{\text{rot},o}$
KIC 3341457	EB	1.859(1)	1.893(7)	0.982(4)
KIC 7596250	EB	1.1876(7)	1.185(4)	1.003(4)
KIC 7621649	SPOT	0.7745(4)	0.7802(6)	0.9928(9)
KIC 9652302	SPOT	0.9147(6)	0.910(2)	1.005(3)
KIC 9716563	SPOT	0.9081(9)	0.90(2)	1.01(2)
KIC 10423501	SPOT	0.8420(6)	0.841(4)	1.001(4)

2014; García et al. 2014; Balona 2017), and deducing surface rotation by tidal locking in binaries (e.g. Kallinger et al. 2017; Guo et al. 2017; Zhang et al. 2018). A signal caused by spots is common for low-mass stars with convective envelopes. However, only 10% of intermediate- and high-mass stars show detectable magnetic fields based on Zeeman splitting (Donati & Landstreet 2009; Wade et al. 2016), which implies a lack of spot activity. Nevertheless, Van Reeth et al. (2018) detected rotational modulations from 8 stars among 68 γ Dor stars, whose detection percentage is consistent with the magnetic observation.

The signal of rotational modulation in frequency is located between g- and r-modes and we have searched for it in all stars. We follow the criteria reported by Van Reeth et al. (2018) to inspect the surface rotation. The criteria are: (1)

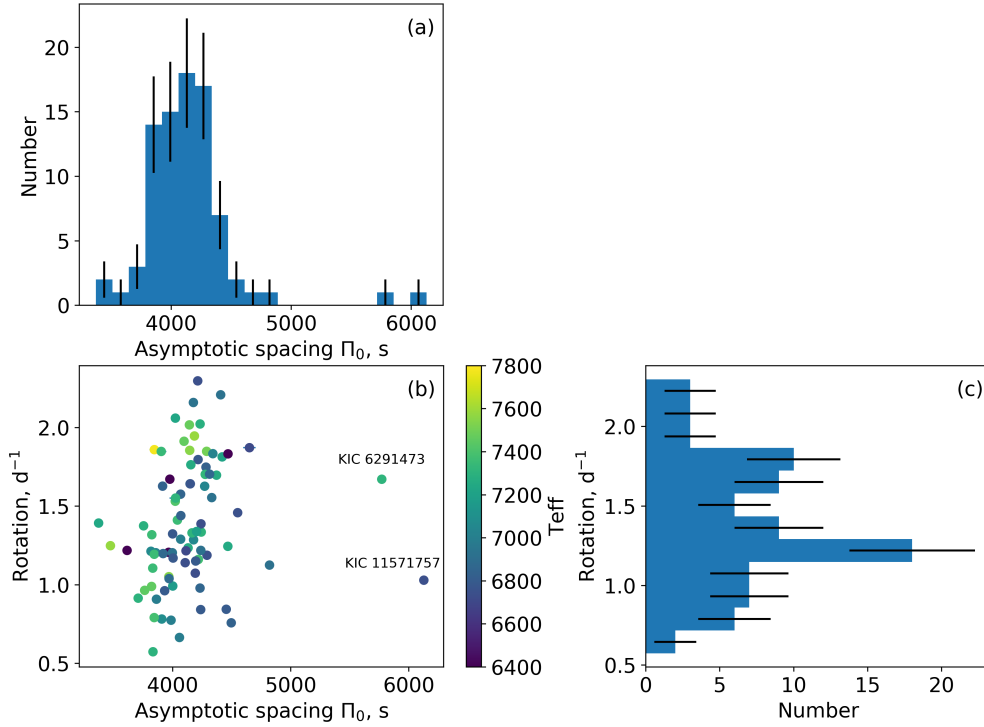


Figure 11. The asymptotic spacing Π_0 and the near-core rotation f_{rot} . The colour bar is the effective temperature. Uncertainties of histograms are the square roots of numbers assuming they are Poisson distributed.

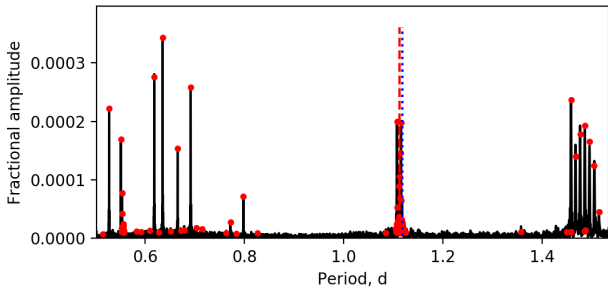


Figure 12. The pulsation and surface rotation of KIC 9716563. Three peak groups are seen. The peak groups at 1.11 d is the signal of the surface modulation. The blue dotted line (overlapped with the red dotted line) displays the near-core rotation while the red dashed line shows the surface rotation, which is the mean of the peaks. The periods below 0.8 d are $l = 1, m = 1$ g-modes and the periods above 1.4 d are $k = -2, m = -1$ r-modes.

the S/N of the peak is larger than 4; (2) the second harmonic $2f$ is found; (3) the selected frequency is part of an isolated group of frequencies, since the lifetime of spot is assumed to be shorter than the Kepler data span; (4) the peak should stand between g- and r-modes. We found six stars which have a signal of rotational modulation that satisfies all these conditions. Table 2 lists the near-core and surface rotation rates ($f_{\text{rot},i}$ and $f_{\text{rot},o}$) and their ratio. KIC 3341457 and KIC 7596250 are classified as eclipsing binaries or ellipsoidal variables (Kirk et al. 2016) while the modulations

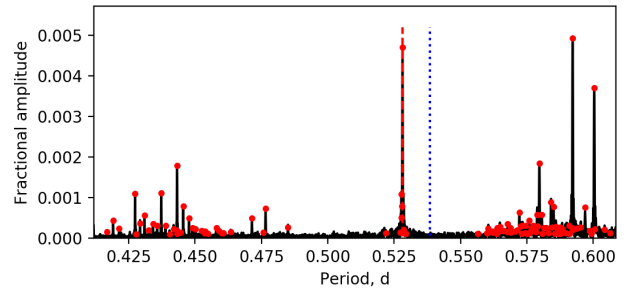


Figure 13. The pulsation and surface rotation of KIC 3341457. This star shows a large discrepancy between the near-core rotation period (blue dotted line) and the orbital period (red dashed line). It implies a radial differential rotation.

for the other three stars are likely caused by spots. Only KIC 3341457 has an obvious differential rotation. The other four stars are quasi-rigidly rotating, as their derived $f_{\text{rot},i}$ and $f_{\text{rot},o}$ values are close to each other.

Appendix B contains their periodograms. We use KIC 9716563 as an example. Figure 12 displays the periodogram of KIC 9716563. The peaks at periods below 0.8 d belong to the $l = 1, m = 1$ g-modes and the peaks at periods above 1.4 d are $k = 2, m = 1$ r-modes. There is a region between g- and r-modes in which we did not find any extra peaks. However, a strong peak group appears at 1.11 d, which is roughly equal to the near-core rotation rate 1.102 ± 0.001 d. We identified this peak group as the surface

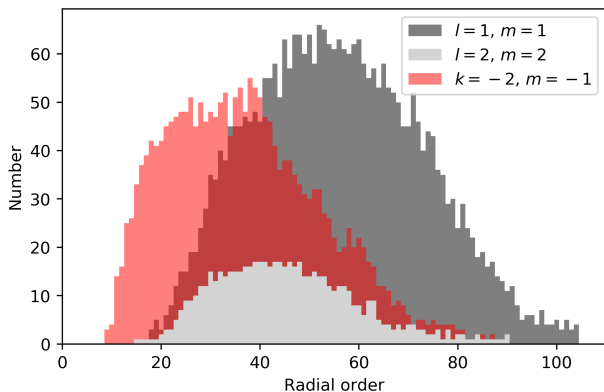


Figure 14. The distributions of radial orders. The black, white and red areas stand for dipole, quadrupole g-modes and r-modes.

modulation, which is likely to be caused by surface spot. The surface modulation shows multiple peaks, indicating the spot lifetime is shorter than the data span, the spot size varies with time, or there is latitude differential rotation. The amplitude caused by the spot is similar to the strongest g and r-mode oscillations ($\sim 0.2\%$ of the mean flux).

KIC 3341457 is the only star which shows differential rotation. It is identified as ‘an ellipsoidal variable or a system with an uncertain classification’ with orbital period of 0.5281792 d (Matijević et al. 2012; Kirk et al. 2016). Figure 13 displays the periodogram of KIC 3341457. The orbital effect generates a peak group at 0.528 d. However, the near-core rotation derived from the g- and r-modes is 0.538 d, 2% longer than the surface rotation. Considering the short orbital period, the stellar surface is likely tidally locked hence this star has a non-uniform rotational profile.

KIC 7596250 is also identified as a binary but its orbital period is equal to the near-core rotation period. So KIC 7596250 is rigidly rotating, assuming its surface is tidally locked.

Although spot activity is generally weak in intermediate-mass stars, it is still possible to find surface modulations in a few cases. Apart from the spot activity, binary effect also involves a signal corresponding to the orbital period which implies surface rotation, assuming the surface is tidally locked. According to our results and those from Van Reeth et al. (2018), most main-sequence stars have uniform rotation profiles, while the components in binary systems are more likely to be differentially rotating, due to the tidal locking effect. Many theoretical mechanisms can cause the differential rotation, such as the internal gravity waves (Aerts et al. 2018a), magnetic fields (e.g. Mathis & Zahn 2005; Prat et al. 2019), and tides (e.g. Lurie et al. 2017; Zhang et al. 2018). KIC 3341457 is an excellent star for modelling angular momentum transport mechanisms.

4.8 Radial order distribution

The radial orders of pulsations in a slow rotator can be estimated as the period divided by the period spacing, $P/\Delta P$, because of the asymptotic spacing in Eq. 6. However, rota-

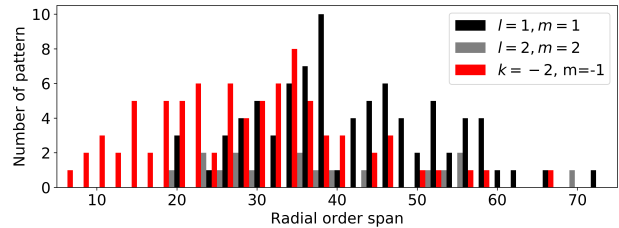


Figure 15. The radial order span of the g- and r-modes. Most of patterns show ~ 30 radial order length. But several g-modes patterns show extremely long radial order spans, even up to 70.

tion changes the period spacing, hence this becomes invalid for most γ Dor stars. We used the TAR fit results to get more accurate estimates of the radial orders. Fig. 14 displays the radial order distributions of the excited modes for the whole sample.

For dipole g-modes, the most likely radial order is ~ 55 . The distribution shows a spread with Full-Width-at-Half-Maximum (FWHM) of ~ 50 . The lowest n is 18 while the highest one is 103. For quadrupole g-modes, the range in radial orders spans from 15 to 83 with FWHM of ~ 30 . The most frequent radial order is ~ 40 , slightly lower than for dipole g-modes, which is possibly because identification of quadrupole modes is more difficult, since the period region overlaps with the harmonics of dipole g modes, and the peaks are generally crowded. This may lead to missing the highest order modes.

Both the dipole and quadrupole g modes are symmetrically distributed. However, the distribution of radial orders of r-modes is asymmetric. Most r-modes peaks have the radial order between ~ 13 and ~ 53 with FWHM of ~ 40 , which is lower than the g modes.

Figure 15 summarises the pattern lengths of the dipole, quadrupole g-modes and r-modes, determined as the difference between the largest and smallest radial orders in each star. For the dipole g modes (black histogram), patterns typically span ~ 35 . Of those, KIC 11571757 has the longest period spacing pattern spanning 73 modes, as shown in the online supplementary material. For the quadrupole g-mode patterns (grey), the typical length is similar to the dipole one. For the r-modes (red), the pattern is typically shorter than for g-modes. The distribution of r-modes shows the excess over that of g-modes when the length is smaller than 30. Of those, KIC 5640438 shows the longest r-mode period spacing pattern, which spans 67 radial orders.

To summarise, the distributions of excited radial orders in g-modes is symmetric with centre of $n \sim 40$. There are more low-radial-order r-modes than g-modes, and their distribution is asymmetric. The excited modes generally span tens of radial orders in both g- and r-modes. Rossby mode patterns show lower radial orders and shorter lengths than the g-mode patterns.

5 CONCLUSIONS

We report 82 γ Dor stars in which the period spacing patterns of both g- and r-modes are seen, which forms the

largest sample of γ Dor stars with r-modes. The period spacing changes approximately linearly with period due to the near-core rotation but shows some fluctuations caused by chemical composition gradients. In each star, the g- and r-modes have similar period spacings (around several hundred seconds), but the mean periods of r-modes are generally twice those of g-modes. We observed some turning points in ΔP for r-modes in several stars, caused by the rapid change of the eigenvalue λ . By fitting a straight line to ΔP versus P , we find that the slope correlates negatively with the mean period in r-modes.

The traditional approximation of rotation (TAR) was used to fit the observed patterns and calculate the near-core rotation rates. The fit matched the observed patterns well, and the near-core rotation rate (f_{rot}) and the asymptotic spacing (Π_0) were constrained accurately. Most of the 82 stars have rotation frequencies between 1 and 2d^{-1} , with Π_0 around 4000 s. We noticed six stars which have surface modulations caused by spots or the ellipsoidal variability in a binary system. Of those, five stars rotate uniformly while KIC 3341457 has a differential core-to-surface rotation. This is consistent with the previous observations that most main-sequence stars rotate quasi-rigidly while components in binary systems are more likely to have non-uniform rotation profile. The radial orders of excited modes display different distributions for the dipole g-modes, quadrupole g-modes, and r-modes. Most g-modes appear around $n \sim 55$, while the radial orders of r-modes are likely to be between 13 and 50, generally lower than those of g-modes.

Our sample is very useful for understanding the physics of rotation and angular momentum transport in main sequence stars, and can place much needed constraints on diffusive mixing and chemical gradients, whilst also providing stellar ages.

ACKNOWLEDGEMENT

The research was supported by an Australian Research Council DP grant DP150104667. Funding for the Stellar Astrophysics Centre is provided by the Danish National Research Foundation (Grant DNR106). This work has made use of data from the European Space Agency (ESA) mission *Gaia* (<https://www.cosmos.esa.int/gaia>), processed by the *Gaia* Data Processing and Analysis Consortium (DPAC, <https://www.cosmos.esa.int/web/gaia/dpac/consortium>). Funding for the DPAC has been provided by national institutions, in particular the institutions participating in the *Gaia* Multilateral Agreement.

REFERENCES

- Aerts C., Molenberghs G., Kenward M. G., Neiner C., 2014, *ApJ*, **781**, 88
- Aerts C., Mathis S., Rogers T., 2018a, preprint, ([arXiv:1809.07779](https://arxiv.org/abs/1809.07779))
- Aerts C., et al., 2018b, *ApJS*, **237**, 15
- Andersson N., 1998, *ApJ*, **502**, 708
- Asplund M., Grevesse N., Sauval A. J., Scott P., 2009, *ARA&A*, **47**, 481
- Ballot J., Lignières F., Prat V., Reese D. R., Rieutord M., 2012, in Shibahashi H., Takata M., Lynas-Gray A. E., eds, *Astronomical Society of the Pacific Conference Series Vol. 462, Progress in Solar/Stellar Physics with Helio- and Asteroseismology*. p. 389 ([arXiv:1109.6856](https://arxiv.org/abs/1109.6856))
- Balona L. A., 2017, *MNRAS*, **467**, 1830
- Balona L. A., Krisciunas K., Cousins A. W. J., 1994, *MNRAS*, **270**, 905
- Bedding T. R., Murphy S. J., Colman I. L., Kurtz D. W., 2015, in *European Physical Journal Web of Conferences*. p. 01005 ([arXiv:1411.1883](https://arxiv.org/abs/1411.1883)), doi:10.1051/epjconf/201510101005
- Benomar O., et al., 2018, *Science*, **361**, 1231
- Berthomieu G., Provost J., 1983, *A&A*, **122**, 199
- Borucki W. J., et al., 2010, *Science*, **327**, 977
- Bouabid M.-P., Montalbán J., Miglio A., Dupret M.-A., Grigahcène A., Noels A., 2011, *A&A*, **531**, A145
- Bouabid M.-P., Dupret M.-A., Salmon S., Montalbán J., Miglio A., Noels A., 2013, *MNRAS*, **429**, 2500
- Brown E. F., Ushomirsky G., 2000, *ApJ*, **536**, 915
- Cazorla C., Nazé Y., Morel T., Georgy C., Godart M., Langer N., 2017, *A&A*, **604**, A123
- Christophe S., Ballot J., Ouazzani R.-M., Antoci V., Salmon S. J. A. J., 2018, *A&A*, **618**, A47
- Cousins A. W. J., Warren P. R., 1963, *Monthly Notes of the Astronomical Society of South Africa*, **22**, 65
- Couvidat S., García R. A., Turck-Chièze S., Corbard T., Henney C. J., Jiménez-Reyes S., 2003, *ApJ*, **597**, L77
- Degroote P., et al., 2011, *A&A*, **536**, A82
- Donati J.-F., Landstreet J. D., 2009, *ARA&A*, **47**, 333
- Dupret M.-A., Grigahcène A., Garrido R., Gabriel M., Scuflaire R., 2005, *A&A*, **435**, 927
- Eckart C., 1960, *Hydrodynamics of oceans and atmospheres*. Pergamon Press, Oxford, <http://cds.cern.ch/record/1975181>
- Foreman-Mackey D., Hogg D. W., Lang D., Goodman J., 2013, *PASP*, **125**, 306
- Gaia Collaboration et al., 2016, *A&A*, **595**, A1
- Gaia Collaboration et al., 2018a, preprint, ([arXiv:1804.09382](https://arxiv.org/abs/1804.09382))
- Gaia Collaboration et al., 2018b, *A&A*, **616**, A1
- Gaia Collaboration et al., 2018c, *A&A*, **616**, A10
- García R. A., et al., 2014, *A&A*, **572**, A34
- Guo Z., Gies D. R., Matson R. A., 2017, *ApJ*, **851**, 39
- Hatta Y., Sekii T., Takata M., Kurtz D. W., 2019, *ApJ*, **871**, 135
- Kallinger T., et al., 2017, *A&A*, **603**, A13
- Kaye A. B., Handler G., Krisciunas K., Poretti E., Zerbi F. M., 1999, *PASP*, **111**, 840
- Keen M. A., Bedding T. R., Murphy S. J., Schmid V. S., Aerts C., Tkachenko A., Ouazzani R.-M., Kurtz D. W., 2015, *MNRAS*, **454**, 1792
- Kirk B., et al., 2016, *AJ*, **151**, 68
- Kjeldsen H., 2003, *Ap&SS*, **284**, 1
- Koch D. G., et al., 2010, *ApJ*, **713**, L79
- Kurtz D. W., Saio H., Takata M., Shibahashi H., Murphy S. J., Sekii T., 2014, *MNRAS*, **444**, 102
- Kurtz D. W., Shibahashi H., Murphy S. J., Bedding T. R., Bowman D. M., 2015, *MNRAS*, **450**, 3015
- Lee U., Saio H., 1987, *MNRAS*, **224**, 513
- Lee U., Saio H., 1997, *ApJ*, **491**, 839
- Li G., Bedding T. R., Murphy S. J., Van Reeth T., Antoci V., Ouazzani R.-M., 2019, *MNRAS*, **482**, 1757
- Liang Z.-C., Gizon L., Birch A. C., Duvall Jr T. L., 2018, arXiv e-prints,
- Löptien B., Gizon L., Birch A. C., Schou J., Proxauf B., Duvall T. L., Bogart R. S., Christensen U. R., 2018, *Nature Astronomy*, **2**, 568
- Lovelace R. V. E., Romanova M. M., 2014, *Fluid Dynamics Research*, **46**, 041401
- Lurie J. C., et al., 2017, *AJ*, **154**, 250

Maeder A., 2009, Physics, Formation and Evolution of Rotating Stars, doi:10.1007/978-3-540-76949-1.

Mathis S., Zahn J.-P., 2005, *A&A*, **440**, 653

Mathis S., Decressin T., Eggenberger P., Charbonnel C., 2013, *A&A*, **558**, A11

Mathur S., et al., 2017, *ApJS*, **229**, 30

Matijević G., Prša A., Orosz J. A., Welsh W. F., Bloemen S., Barclay T., 2012, *AJ*, **143**, 123

Mazumdar A., et al., 2014, *ApJ*, **782**, 18

McIntosh S. W., Cramer W. J., Pichardo Marcano M., Leamon R. J., 2017, *Nature Astronomy*, **1**, 0086

McQuillan A., Mazeh T., Aigrain S., 2014, *ApJS*, **211**, 24

Miglio A., Montalbán J., Noels A., Eggenberger P., 2008, *MNRAS*, **386**, 1487

Mombarg J. S. G., Van Reeth T., Pedersen M. G., Molenberghs G., Bowman D. M., Johnston C., Tkachenko A., Aerts C., 2019, *MNRAS*,

Montgomery M. H., Odonoghue D., 1999, Delta Scuti Star Newsletter, **13**, 28

Murphy S. J., Fossati L., Bedding T. R., Saio H., Kurtz D. W., Grassitelli L., Wang E. S., 2016, *MNRAS*, **459**, 1201

Murphy S. J., Hey D., Van Reeth T., Bedding T. R., 2019, *MNRAS*,

Ouazzani R.-M., Salmon S. J. A. J., Antoci V., Bedding T. R., Murphy S. J., Roxburgh I. W., 2017, *MNRAS*, **465**, 2294

Papaloizou J., Pringle J. E., 1978, *MNRAS*, **182**, 423

Pápics P. L., et al., 2017, *A&A*, **598**, A74

Paxton B., Bildsten L., Dotter A., Herwig F., Lesaffre P., Timmes F., 2011, *ApJS*, **192**, 3

Pedlosky J., 1982, Geophysical fluid dynamics

Prat V., Mathis S., Augustson K., Lignières F., Ballot J., Alvan L., Brun A. S., 2018, *A&A*, **615**, A106

Prat V., Mathis S., Buysschaert B., Van Beeck J., Bowman D. M., Aerts C., Neiner C., 2019, arXiv e-prints,

Provost J., Berthomieu G., Rocca A., 1981, *A&A*, **94**, 126

Rossby C. G., 1939, *J. Mar. Res.*, **2**, 38

Royer F., Zorec J., Gómez A. E., 2007, *A&A*, **463**, 671

Saio H., 1982, *ApJ*, **256**, 717

Saio H., Kurtz D. W., Takata M., Shibahashi H., Murphy S. J., Sekii T., Bedding T. R., 2015, *MNRAS*, **447**, 3264

Saio H., Kurtz D. W., Murphy S. J., Antoci V. L., Lee U., 2018a, *MNRAS*, **474**, 2774

Saio H., Bedding T. R., Kurtz D. W., Murphy S. J., Antoci V., Shibahashi H., Li G., Takata M., 2018b, *MNRAS*, **477**, 2183

Schmid V. S., Aerts C., 2016, *A&A*, **592**, A116

Screen J. A., Simmonds I., 2014, *Nature Climate Change*

Shibahashi H., 1979, *PASJ*, **31**, 87

Stumpe M. C., Smith J. C., Catanzarite J. H., Van Cleve J. E., Jenkins J. M., Twicken J. D., Girouard F. R., 2014, *PASP*, **126**, 100

Thompson M. J., et al., 1996, *Science*, **272**, 1300

Townsend R. H. D., 2003, *MNRAS*, **340**, 1020

Townsend R. H. D., 2005, *MNRAS*, **360**, 465

Townsend R. H. D., Teitler S. A., 2013, *MNRAS*, **435**, 3406

Triana S. A., Moravveji E., Pápics P. I., Aerts C., Kawaler S. D., Christensen-Dalsgaard J., 2015, *ApJ*, **810**, 16

Van Reeth T., et al., 2015a, *ApJS*, **218**, 27

Van Reeth T., et al., 2015b, *A&A*, **574**, A17

Van Reeth T., Tkachenko A., Aerts C., 2016, *A&A*, **593**, A120

Van Reeth T., et al., 2018, *A&A*, **618**, A24

Wade G. A., Petit V., Grunhut J. H., Neiner C., MiMeS Collaboration 2016, in Sigut T. A. A., Jones C. E., eds, *Astronomical Society of the Pacific Conference Series Vol. 506, Bright Emisseries: Be Stars as Messengers of Star-Disk Physics*. p. 207

White T. R., Bedding T. R., Stello D., Christensen-Dalsgaard J., Huber D., Kjeldsen H., 2011, *ApJ*, **743**, 161

Zaqarashvili T. V., Oliver R., Hanslmeier A., Carbonell M.,

Ballester J. L., Gachechiladze T., Usoskin I. G., 2015, *ApJ*, **805**, L14

Zhang X. B., Fu J. N., Luo C. Q., Ren A. B., Yan Z. Z., 2018, *ApJ*, **865**, 115

APPENDIX A: PERIOD SPACING DIAGRAMS

We show the period spacing patterns, the sideways échelle diagrams, the TAR fit results, and the posterior distributions of 82 γ Dor stars with gravity modes and Rossby modes patterns. Example diagrams are shown in figs A1 to A3. The figures for the other 81 stars are available as supplementary online material.

APPENDIX B: SURFACE MODULATIONS

We present six stars with surface modulations in this appendix. KIC 3341457 displays a strong radial differential rotation while the other five stars show uniform rotation.

This paper has been typeset from a $\text{\TeX}/\text{\LaTeX}$ file prepared by the author.

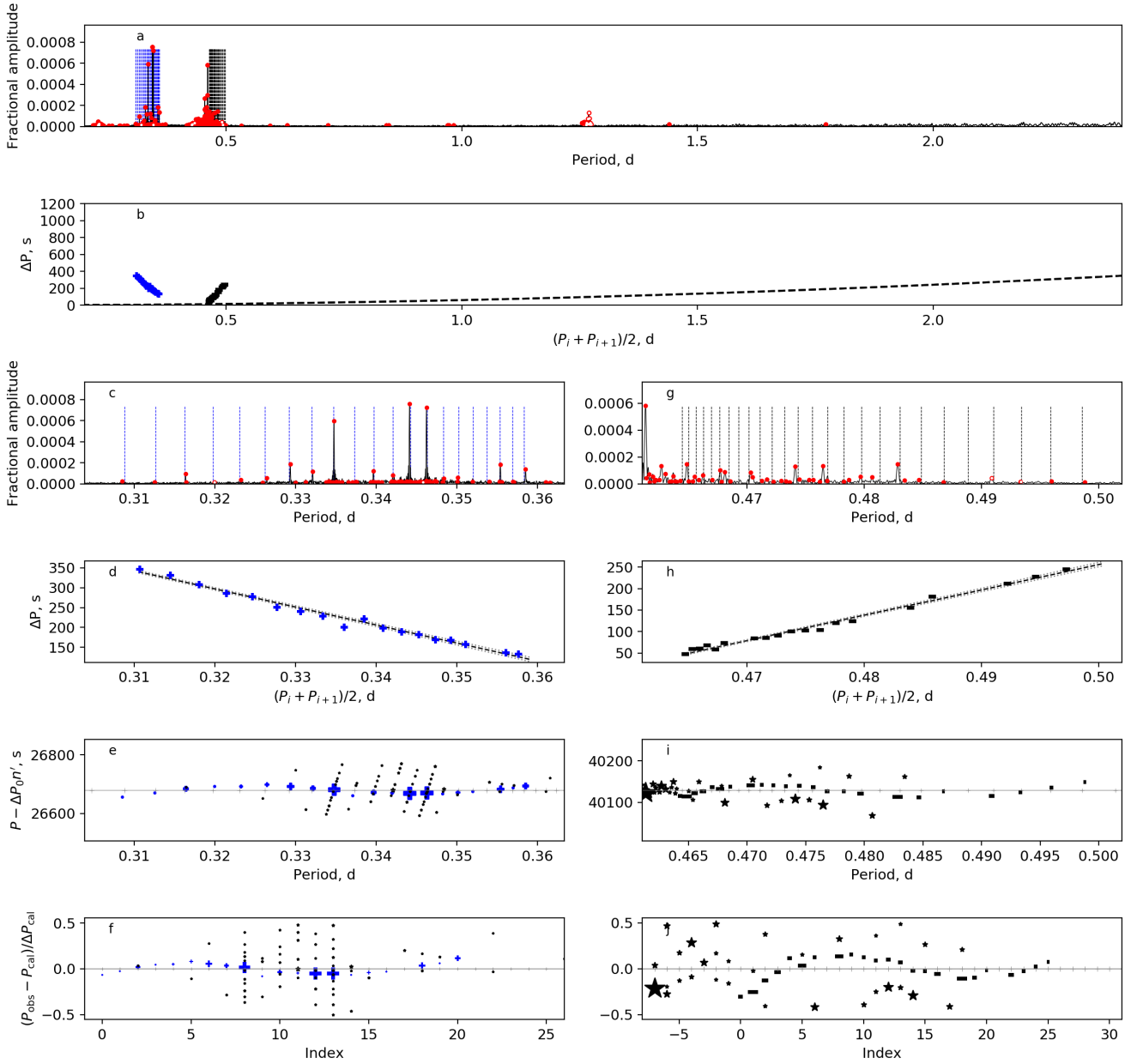


Figure A1. The g and r-mode patterns of KIC 6301745. Panel a: the amplitude spectrum with x-axis of period. The solid red circles present the detected independent frequencies while the open red circles show the combination frequencies. The vertical dashed lines are the linear fits for each pattern. The x-axis range is set from 0.2d to 2.4d for consistency for all stars. There are two period spacing patterns. The blue one on the left is the $l = 1, m = 1$ g-modes while the black one on the right is the $k = -2, m = -1$ r-modes. Panel b: the period spacing patterns of KIC 6301745. The linear fits and uncertainties are shown by the black and grey dashed lines. The blue plus symbols are the g-modes and the black minus symbols are the r-modes. The dashed line is the period resolution. Panels c and d: the detail of the spectrum and period spacing pattern of g-modes. Panel e: the sideways échelle diagram of the g pattern. Panel f: the normalised sideways échelle diagram of the g-modes pattern. Panels g to j: same but for the r-mode pattern.

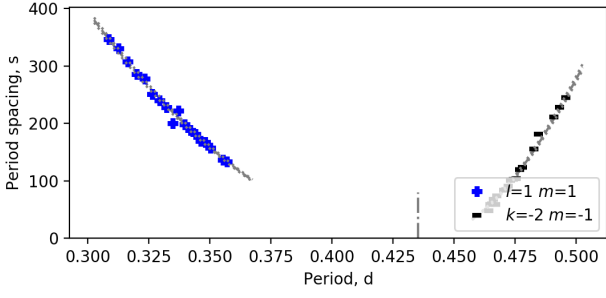


Figure A2. The TAR fit of KIC 6301745. The blue plus symbols show the $l = 1, m = 1$ gravity modes and the black minus symbols show the $k = -2, m = -1$ Rossby modes. The dashed grey curves display the best-fitted result. The error margins are plotted by the dotted lines. The vertical dashed line denotes the fitted rotation period.

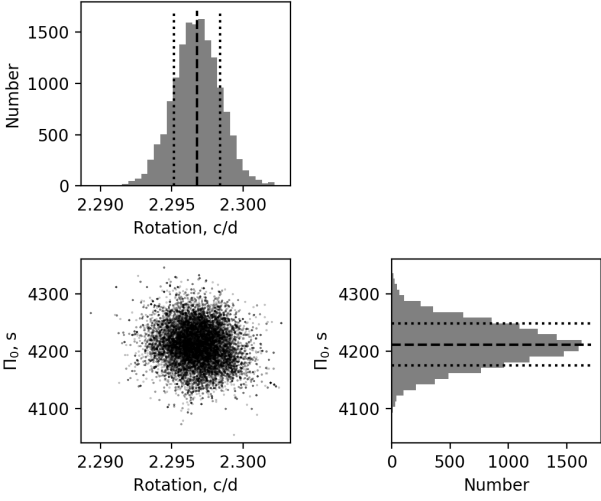


Figure A3. The posterior distributions for the TAR fit to KIC 6301745 using eq. 9. The dashed lines are the medians and the dotted lines show the $\pm 1\sigma$ areas.

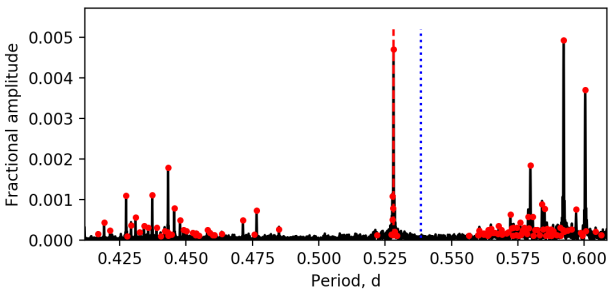


Figure B1. The periodogram and surface rotation of KIC 3341457. The red dots are peaks with $S/N > 4$. The peak groups at 0.528 d is the signal of the surface modulation. The blue dotted line displays the near-core rotation while the red dashed line shows the surface rotation, which is the mean of the peaks.

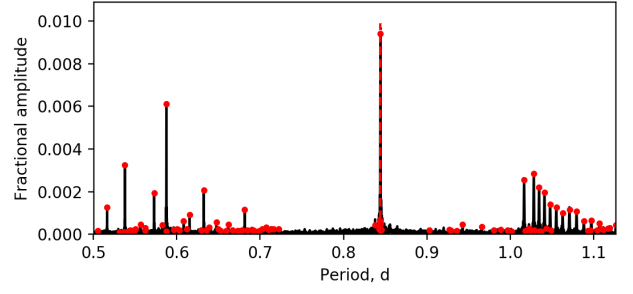


Figure B2. The periodogram and surface rotation of KIC 7596250.

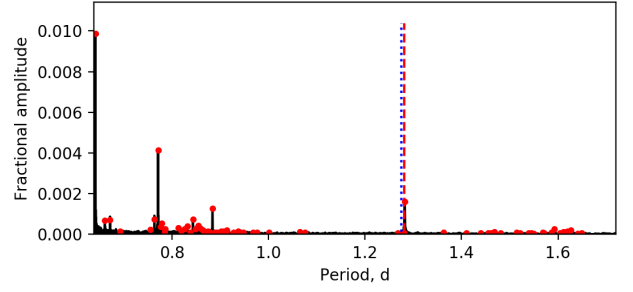


Figure B3. The periodogram and surface rotation of KIC 7621649.

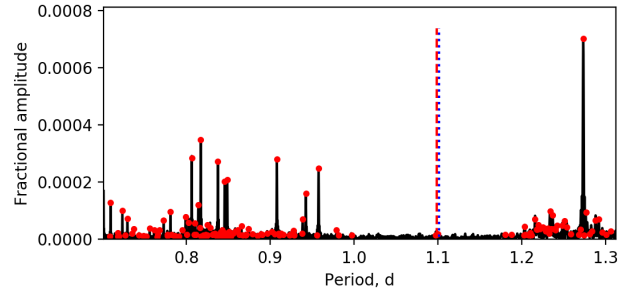


Figure B4. The periodogram and surface rotation of KIC 9652302.

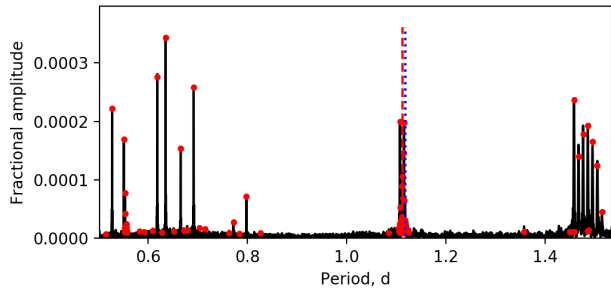


Figure B5. The periodogram and surface rotation of KIC 9716563.

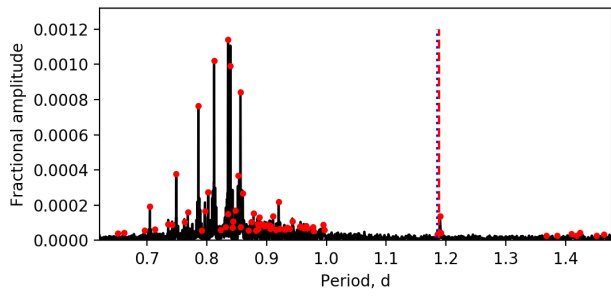


Figure B6. The periodogram and surface rotation of KIC 10423501.